

## Global Climate Simulation with the University of Wisconsin Global Hybrid Isentropic Coordinate Model

TODD K. SCHAACK, TOM H. ZAPOTOCNY, ALLEN J. LENZEN, AND DONALD R. JOHNSON

*Space Science and Engineering Center, University of Wisconsin—Madison, Madison, Wisconsin*

(Manuscript received 23 May 2003, in final form 14 January 2004)

### ABSTRACT

The purpose of this study is to briefly describe the global atmospheric University of Wisconsin (UW) hybrid isentropic–eta coordinate (UW  $\theta$ – $\eta$ ) model and document results from a 14-yr climate simulation. The model, developed through modification of the UW hybrid isentropic–sigma ( $\theta$ – $\sigma$ ) coordinate model, employs a vertical coordinate that smoothly varies from terrain following at the earth's surface to isentropic coordinates in the middle to upper troposphere. The UW  $\theta$ – $\eta$  model eliminates the discrete interface in the UW  $\theta$ – $\sigma$  model between the PBL expressed in sigma coordinates and the free atmosphere expressed in isentropic coordinates. The smooth transition of the modified model retains the excellent transport characteristics of the UW  $\theta$ – $\sigma$  model while providing for straightforward application of data assimilation techniques, use of higher-order finite-difference schemes, and implementation on massively parallel computing platforms.

This study sets forth the governing equations and describes the vertical structure employed by the UW  $\theta$ – $\eta$  model after which the results from a 14-yr climate simulation detail the model's simulation capabilities. Relative to reanalysis data and other fields, the dominant features of the global circulation, including seasonal variability, are well represented in the simulations, thus demonstrating the viability of the hybrid model for extended-length integrations. Overall the study documents that no insurmountable barriers exist to simulation of climate utilizing hybrid isentropic coordinate models. Additional results from two numerical experiments examining conservation demonstrate a high degree of numerical accuracy for the UW  $\theta$ – $\eta$  model in simulating reversibility and potential vorticity transport over a 10-day period that corresponds with the global residence time of water vapor.

### 1. Introduction

A key scientific challenge that has emerged over the past several decades is the issue of human impact on the earth's climate. The resulting concerns have focused attention on the need for comprehensive climate predictions. The diversity of results from past and current climate simulations has highlighted the considerable uncertainty that exists due to the simplifications that are introduced to make the global simulation of climate tractable. Considerable effort has been devoted to the attempt to advance climate simulation through increased resolution and revised parameterization. These endeavors have advanced the realism of climate simulations and deserve continued effort. However, such efforts alone have not ascertained unequivocal accuracies needed to resolve regional climate change with respect to the atmosphere's hydrologic and chemical processes, and other anthropogenic impacts. Ensuring the accuracy of the transports of energy, entropy, water vapor, and

other trace constituents is fundamental to advancing the modeling of thermodynamic processes that force the climate state (Arakawa and Lamb 1977; Arakawa and Hsu 1990; Johnson 1997; Egger 1999).

A relatively recent development in NWP, climate modeling, and data assimilation is the formulation and application of models expressed in isentropic or hybrid isentropic coordinates (Benjamin 1989; Hsu and Arakawa 1990; Zhu et al. 1992; Thuburn 1993; Bleck and Benjamin 1993; Pierce and Fairlie 1993; Arakawa and Konor 1994; Konor et al. 1994; Benjamin et al. 1994; Chipperfield et al. 1995; Zhu and Schneider 1997; Zhu 1997; Konor and Arakawa 1997; Zapotocny et al. 1994, 1996, 1997a,b; Johnson and Yuan 1998; Reames and Zapotocny 1999a,b; Webster et al. 1999; Johnson et al. 2000, 2002). Many of the preceding authors (e.g., Hsu and Arakawa 1990; Webster et al. 1999; Arakawa 2000) discuss the advantages and disadvantages of modeling in isentropic coordinates. The disadvantages of modeling in isentropic coordinates, such as the lack of resolution in unstable boundary layer regions and the intersection of model surfaces with the surface of the earth, are largely ameliorated by using a hybrid isentropic coordinate system in which the PBL is represented by sigma coordinates (Bleck 1978).

---

*Corresponding author address:* Todd K. Schaack, Space Science and Engineering Center, University of Wisconsin—Madison, 1225 W. Dayton St., Madison, WI 53706.  
E-mail: todd.schaack@ssec.wisc.edu

Numerical integration in isentropic coordinates at the global scale provides the potential for improved simulation of the long-range transport of thermodynamic properties including water substances, clouds, atmospheric constituents, etc. (Johnson et al. 1993, 2000, 2002). A key advantage results from the relation between Lagrangian sources of entropy and diabatic vertical mass transport relative to isentropic surfaces. Apart from the localized regions of moist convection in the free atmosphere and turbulent energy exchange in the PBL, the sources/sinks of entropy are minimal and the transport of water vapor and other trace constituents lies within inclined isentropic layers. Discretization errors associated with the vertical transport of properties within a stratified atmosphere are minimized and the difficulties associated with vertical exchange of both fundamental atmospheric properties and key constituents remain minimal in isentropic coordinates relative to sigma coordinates. This attribute is especially beneficial in the simulation of quasi-horizontal exchange processes of extratropical latitudes since baroclinic amplification is primarily an isentropic process. The increased accuracy in baroclinic regimes translates to improved simulation of stratospheric-tropospheric exchange and the simulation of clouds including hydrologic, chemical, and other constituents (Zapotocny et al. 1996, 1997a,b).

Zhu and Schneider (1997) and Webster et al. (1999) have demonstrated the capability of hybrid isentropic coordinate models for long-term integration. Both studies compared simulations from a control hybrid sigma-pressure ( $\sigma$ - $p$ ) coordinate model with corresponding results from a hybrid sigma-isentropic ( $\sigma$ - $\theta$ ) coordinate model in which the coordinate changed from sigma at the earth's surface to isentropic (Webster et al. 1999) or nearly isentropic (Zhu and Schneider 1997) in the upper troposphere and lower stratosphere. Both studies found improvements in the simulated stratospheric and upper-tropospheric circulation when using a hybrid ( $\sigma$ - $\theta$ ) relative to a control ( $\sigma$ - $p$ ) coordinate model. One key improvement was a substantial reduction of high-latitude cold biases in the lower stratosphere/upper troposphere in the hybrid isentropic coordinate simulations. In a continuation of Zhu and Schneider (1997), Zhu (1997) found significant improvement in simulation of the tropical large-scale circulation, water vapor transport, and precipitation with the  $\sigma$ - $\theta$  coordinate relative to the  $\sigma$ - $p$  coordinate. Suggested reasons for the improved simulation in hybrid isentropic coordinates included more accurate advection and vertical propagation and dissipation of planetary waves, results that are consistent with Johnson's (1997) theoretical study. Johnson (1997) documented that the use of entropy as the thermodynamic variable in isentropic coordinates eliminates positive definite aphysical sources of entropy stemming from discrete numerics and energy advection that occur in models expressed in other coordinate systems.

In a series of studies to document the relative capabilities of models, the long-range transports of water

vapor, inert trace constituents, and potential vorticity were examined by comparing simulations from the University of Wisconsin (UW) hybrid isentropic-sigma ( $\theta$ - $\sigma$ ) model, a companion UW  $\sigma$  model, and the National Center for Atmospheric Research (NCAR) Community Climate Models (CCM2 and CCM3; Johnson et al. 2000, 2002; Zapotocny et al. 1994, 1996, 1997a,b). The UW  $\theta$ - $\sigma$  model with approximately 85% of the atmosphere represented by isentropic coordinates simulated the long-range transport of these properties to a higher degree of accuracy than the aforementioned grid-point or Eulerian spectral models based on sigma coordinates. The comparisons verified the potential for improved simulation of condensation processes, precipitation, clouds, cloud-radiative feedback, surface energy balance, and therefore global and regional climate with hybrid isentropic models.

The earlier numerical experiments established the credibility of the UW  $\theta$ - $\sigma$  model in simulating transport processes throughout the entire model domain. However, experimentation revealed that for extended integrations, the centered difference algorithm in the model led to persistent regions of negative mass in some isentropic layers, where excessive borrowing became necessary to maintain a positive mass distribution. The discrete interface between the sigma and isentropic domains of the model also presented difficulties for implementing more advanced numerics and for adapting the model for massively parallel computing. Johnson et al. (2000) also identified a small bias and lack of conservation of equivalent potential temperature associated with transport across the discrete interface in the UW  $\theta$ - $\sigma$  model. These factors limited the application of this model for climate simulation.

Johnson and Yuan (1998) modified the existing UW hybrid  $\theta$ - $\sigma$  channel model (Pierce et al. 1991; Zapotocny et al. 1991; Johnson et al. 1993) to develop a channel model ( $\theta$ - $\eta$ ) with a vertical coordinate that transforms smoothly from terrain following at the earth's surface to isentropic coordinates in the middle to upper troposphere. They conducted an idealized NWP experiment and two additional experiments involving the appropriate conservation of isentropic potential vorticity ( $P_\theta$ ) and equivalent potential temperature ( $\theta_e$ ). The NWP results for the  $\theta$ - $\eta$  and  $\theta$ - $\sigma$  channel models were similar as were the conservation characteristics for  $P_\theta$  and  $\theta_e$  in the middle and upper troposphere where isentropic coordinate representation was common to both models. However, the  $\theta$ - $\eta$  model, with its continuous transition from  $\sigma$  to  $\theta$  coordinates, eliminated truncation errors stemming from the discrete interface and thus was more accurate with respect to conservation of properties in the lower troposphere. These results combined with the earlier-cited investigations regarding relative advantages of modeling in isentropic coordinates provided the impetus to develop the global ( $\theta$ - $\eta$ ) model.

Section 2 provides a description of the global hybrid atmospheric model (hereafter called the UW  $\theta$ - $\eta$  model)

with a vertical coordinate that smoothly varies from terrain following at the earth's surface to isentropic coordinates in the middle to upper troposphere. Section 3 presents results from a 14-yr climate simulation and section 4 provides a summary. The primary goal is to document the capability of the UW  $\theta$ - $\eta$  model for long-term integration needed for simulation of climate and climate change.

## 2. Description of the UW $\theta$ - $\eta$ model

### a. The model equations

The governing transport equations for mass ( $\rho J_\eta$ ), zonal ( $u$ ) and meridional ( $v$ ) components of the wind, specific humidity ( $q$ ), and potential temperature ( $\theta$ ) used in the global hybrid UW  $\theta$ - $\eta$  model are expressed in generalized coordinates (after Johnson 1980), respectively, by

$$\frac{\partial}{\partial t_\eta}(\rho J_\eta) = - \left\{ \frac{1}{a \cos \phi} \left[ \frac{\partial}{\partial \lambda_\eta}(\rho J_\eta u) + \frac{\partial}{\partial \phi_\eta}(\rho J_\eta v \cos \phi) \right] + \frac{\partial}{\partial \eta}(\rho J_\eta \dot{\eta}) \right\}, \quad (1)$$

$$\begin{aligned} \frac{\partial}{\partial t_\eta}(\rho J_\eta u) = & - \left\{ \frac{1}{a \cos \phi} \left[ \frac{\partial}{\partial \lambda_\eta}(\rho J_\eta uu) + \frac{\partial}{\partial \phi_\eta}(\rho J_\eta uv \cos \phi) \right] + \frac{\partial}{\partial \eta}(\rho J_\eta \dot{\eta} u) \right\} + \rho J_\eta \left( f v + \frac{uv \tan \phi}{a} \right) \\ & - \rho J_\eta (a \cos \phi)^{-1} \left( \frac{\partial}{\partial \lambda_\eta} \psi - \pi \frac{\partial}{\partial \lambda_\eta} \theta \right) + \rho J_\eta F_u, \end{aligned} \quad (2)$$

$$\begin{aligned} \frac{\partial}{\partial t_\eta}(\rho J_\eta v) = & - \left\{ \frac{1}{a \cos \phi} \left[ \frac{\partial}{\partial \lambda_\eta}(\rho J_\eta uv) + \frac{\partial}{\partial \phi_\eta}(\rho J_\eta vv \cos \phi) \right] + \frac{\partial}{\partial \eta}(\rho J_\eta \dot{\eta} v) \right\} - \rho J_\eta \left( f u + \frac{u^2 \tan \phi}{a} \right) \\ & - \rho J_\eta a^{-1} \left( \frac{\partial}{\partial \phi_\eta} \psi - \pi \frac{\partial}{\partial \phi_\eta} \theta \right) + \rho J_\eta F_v, \end{aligned} \quad (3)$$

$$\frac{\partial}{\partial t_\eta}(\rho J_\eta q) = - \left\{ \frac{1}{a \cos \phi} \left[ \frac{\partial}{\partial \lambda_\eta}(\rho J_\eta uq) + \frac{\partial}{\partial \phi_\eta}(\rho J_\eta vq \cos \phi) \right] + \frac{\partial}{\partial \eta}(\rho J_\eta \dot{\eta} q) \right\} + \rho J_\eta F_q + \rho J_\eta \dot{q}, \quad (4)$$

$$\frac{\partial}{\partial t_\eta}(\rho J_\eta \theta) = - \left\{ \frac{1}{a \cos \phi} \left[ \frac{\partial}{\partial \lambda_\eta}(\rho J_\eta u\theta) + \frac{\partial}{\partial \phi_\eta}(\rho J_\eta v\theta \cos \phi) \right] + \frac{\partial}{\partial \eta}(\rho J_\eta \dot{\eta} \theta) \right\} + \rho J_\eta \dot{\theta}. \quad (5)$$

In the preceding equations,  $a$  is the earth's radius,  $\phi$  is latitude,  $\lambda$  is longitude,  $\psi$  is the Montgomery streamfunction, and  $\pi$  is the Exner function,  $c_p(p/p_{00})^\kappa$ . Here,  $p_{00}$  equals 1000 hPa and  $\kappa$  is the ratio of the gas constant  $R$  to the specific heat at constant pressure  $c_p$ ;  $F_u$  and  $F_v$  are the zonal and meridional components of the frictional force,  $F_q$  is the diffusion of water vapor, and  $\dot{q}$  is the time rate of change of water vapor per unit mass due to condensation, evaporation, and subgrid-scale diffusion. The pressure gradient terms in the momentum equations are the hydrostatic counterpart of the more general relation

$$a \nabla p + \nabla \phi = \nabla \psi - \pi \nabla \theta,$$

which are computed following Konor and Arakawa (1997) with appropriate transformation to generalized meteorological coordinates (Johnson 1980, 1989).

The Lagrangian source/sink of potential temperature is expressed by

$$\dot{\theta} = \pi^{-1} Q_m, \quad (6)$$

where  $Q_m$  is the rate of specific heat addition. Note that

with  $\dot{\eta}$  equal to  $\dot{\theta}$  in the governing equations of isentropic coordinates, (5) is eliminated by virtue of redundancy with (6) and the mass continuity equation.

### b. The vertical coordinate

The hybrid vertical coordinate  $\eta$  of the global UW  $\theta$ - $\eta$  model is specified to be a continuous monotonic function of height. Three vertically distinct domains of global extent are used to span the hydrostatic model atmosphere. The scaling of the hybrid coordinate by pressure in the lower domain is analogous with the scaling of sigma coordinates. The vertical coordinate of the upper domain has a one-to-one correspondence with potential temperature and is in fact isentropic (i.e.,  $\eta = \theta$ ). The middle (transition) domain provides for a vertical transition from sigma to isentropic coordinates. For convenience, the units of the vertical coordinate throughout the model are expressed as potential temperature (K) even though the vertical coordinate in the lower and transition domains has no immediate relation with potential temperature.

By virtue of the hydrostatic assumption and the convention defined for  $\eta$  coordinates, the mass distribution is specified everywhere by

$$\rho J_{\eta} = -g^{-1} \partial p / \partial \eta. \quad (7)$$

With an indefinite integration of (7) from an arbitrary model surface  $\eta$  to the top surface of the model  $\eta_T$ , the pressure  $p(\eta)$  through the vertical extent of the three domains is given by

$$p(\eta) = p(\eta_T) + g \int_{\eta}^{\eta_T} \rho J_{\eta} d\eta. \quad (8)$$

The lower domain serves as the surface layer of the model and is bounded vertically by  $\eta_s \leq \eta \leq \eta_{\sigma}$ . The lower boundary  $\eta_s$  is contiguous with the earth's surface, while its upper boundary  $\eta_{\sigma}$  serves as the interface surface between the lower and transition domains. Within this domain, the vertical coordinate  $\eta$ , through scaling by the surface pressure  $p(\eta_s)$ , is specified as a linear function of pressure according to

$$\eta = \eta_s \{1 + [p(\eta_s) - p(\eta)]/p(\eta_s)\}. \quad (9)$$

In turn the hydrostatic pressure within the surface layer is specified by

$$p(\eta) = p_s \{1 - [(\eta - \eta_s)/\eta_s]\}. \quad (10)$$

The vertical coordinate within the transition domain  $\eta_{\sigma} \leq \eta \leq \eta_{\theta}$  is defined by

$$\eta = \eta_{\sigma} + \{[p(\eta) - p(\eta_{\theta})]/[p(\eta_{\sigma}) - p(\eta_{\theta})]\}(\eta_{\theta} - \eta_{\sigma}), \quad (11)$$

where  $\eta_{\theta}$  is an isentropic surface serving as the interface between the transition and upper domains of the model. The hydrostatic pressure within the transition domain is defined by

$$p(\eta) = p_{\sigma} - (p_{\sigma} - p_{\theta})[(\eta - \eta_{\sigma})/(\eta_{\theta} - \eta_{\sigma})]. \quad (12)$$

Here, through scaling of the pressure difference  $[p(\eta_{\sigma}) - p(\eta_{\theta})]$  by  $(\eta_{\theta} - \eta_{\sigma})$ , the pressure distribution is in effect a linear function of the pressure. The result is the hydrostatic mass in each incremental layer of the transition domain is invariant vertically, but may vary horizontally.

Finally, within the upper (isentropic) domain ( $\eta_{\theta} \leq \eta \leq \eta_T$ ) with  $\eta$  equal to  $\theta$  everywhere, the hydrostatic pressure is simply defined by

$$p(\eta) = p(\theta), \quad (13)$$

where  $\eta_T$  equal to  $\theta_T$  is the top surface of the model.

The model coordinate smoothly varies from terrain following at the lower boundary at  $\eta_s$  to become completely isentropic for  $\eta \geq \eta_{\theta}$ . For the climate simulation in section 3, the vertical coordinate structure was chosen to maximize vertical resolution in the PBL and to provide a smooth vertical variation of mass in model layers elsewhere. The surface layer was simply specified to be a single layer with  $\eta_s$  and  $\eta_{\sigma}$  equal to 224.0 and 227.0 K,

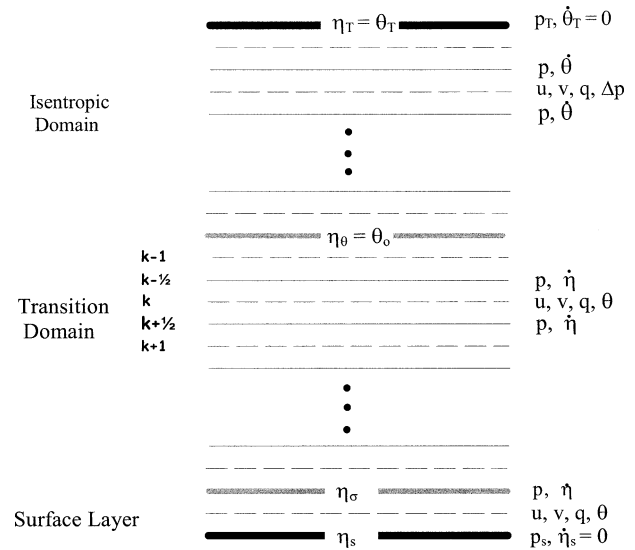


FIG. 1. The vertical grid of the UW  $\theta$ - $\eta$  model with the ordering of model variables indicated for the surface, transition, and isentropic domains. Model layers are denoted by integer indices and layer interfaces denoted by half-integer values.

respectively. The relatively high potential temperature of the interface isentropic surface, with  $\eta_{\theta}$  equal to 336 K, accommodates summertime surface temperatures over the Tibetan Plateau, avoids intersection of the  $\eta$  surface with orography, and provides for sufficient mass to realistically represent transport and physical processes within the surface and transition layers. The model's upper isentropic surface  $\eta_T$  was set equal to 3300 K. The conditions imposed ensure that the hydrostatic mass remains positive definite in all of the discrete layers of the model.

Figure 1 defines the UW  $\theta$ - $\eta$  model vertical grid with model layers denoted by integer indices and layer interfaces denoted by half-integer values. The mass  $\rho J_{\eta}$ , zonal ( $u$ ), and meridional ( $v$ ) components of the wind and specific humidity ( $q$ ) are predicted within layers throughout the model. Potential temperature as a dependent property within the transition and surface domains is predicted within these layers.

Figure 2 presents a meridional cross section along 104°E longitude of the UW  $\theta$ - $\eta$  model vertical structure for day 235 (early August) of the climate simulation presented in section 3. The  $\theta$ - $\eta$  surfaces of the model are represented by solid black lines. For comparison purposes, potential temperatures (dashed lines) are plotted every 10 K, while thick gray lines represent sigma surfaces at 0.1 resolution. The boundary surface  $\eta_s$  equal to 224 follows the earth's surface. At and above the upper boundary of the transition domain at  $\eta_{\theta}$  equal 336 K, model surfaces uniquely correspond with isentropic surfaces. The surface  $\eta_{\theta}$  slopes from near 250 hPa in Northern Hemisphere (NH) high latitudes to 425 hPa in NH middle latitudes, lies near 350 hPa in the Tropics and slopes upward to 160 hPa at the South Pole.

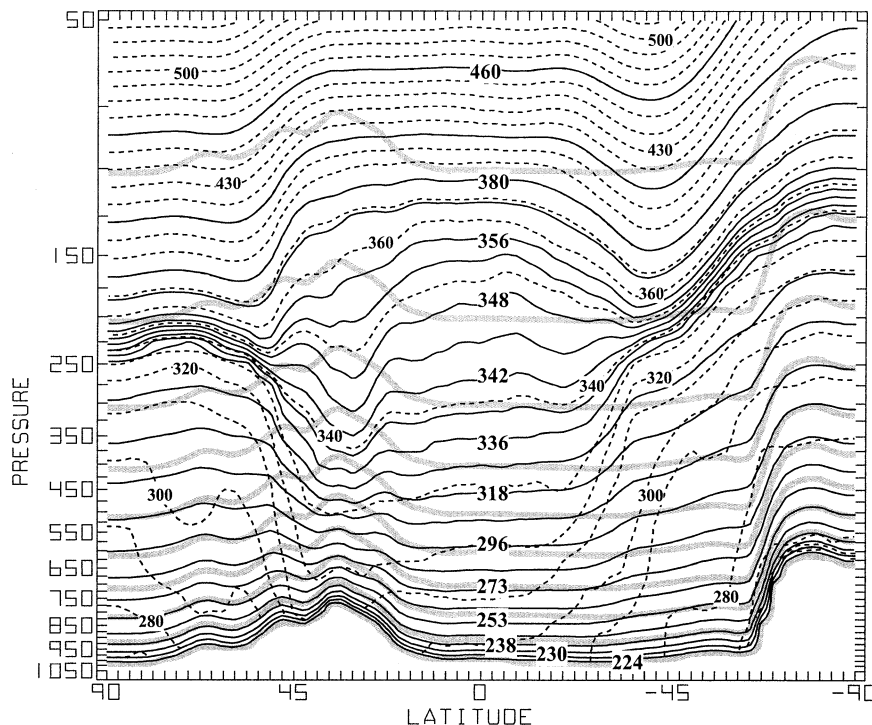


FIG. 2. Meridional cross section between the earth's surface and 50 hPa of UW  $\theta$ - $\eta$  model quasi-horizontal surfaces (solid black), potential temperature (K, dashed) and sigma surfaces (thick gray) along 104°E long for day 235 (early Aug) of the climate simulation. Model coordinates at and above 336 K are isentropic surfaces. The units of the vertical coordinate below the isentropic domain are expressed as potential temperature (K) to facilitate the identification of isentropic surfaces within the upper domain as model coordinates even though such a designation for the vertical coordinate in the lower and middle domains has no immediate relation with potential temperature. Potential temperatures are plotted at 10-K resolution and sigma surfaces at 0.1 resolution.

Through most of the domain, the vertical resolution varies smoothly with the exception of the lower stratosphere just above  $\eta_\theta$  in polar/extratropical latitudes. Here, resolution is enhanced by the isentropic stratification of the low stratosphere. In the transition domain near the interface  $\eta_\theta$  the meridional slopes of the  $\eta$  and  $\theta$  surfaces are in close correspondence, a condition that reflects the scaling of the mass by the pressure distribution on the interface isentropic surface at  $\eta_\theta$  [see Eq. (11)]. Below the middle troposphere the correspondence of  $\eta$  and  $\sigma$  surfaces increases as pressure increases reflecting the transition of the  $\eta$  coordinate from potential temperature at  $\eta_\theta$  to a sigma coordinate at the interface boundary at  $\eta_\sigma$ .

Hybrid rather than isentropic coordinates describe the atmosphere below 336 K. However, the scaling of the  $\eta$  structure in the transition domain with respect to the difference between the pressure at  $p(\eta_\sigma)$  and the isentropic pressure distribution  $p(\eta_\theta)$  at  $\eta_\theta$  has an important consequence. The tendency of pressure at the upper boundary of the transition domain  $\eta_\theta$  is solely determined by the vertically integrated isentropic mass divergence and convergence of the overlying atmosphere and the vertical mass flux through the interface  $\eta_\theta$ . The

result is that the interface surface  $\eta_\theta$  is not only vertically displaced in response to isentropic transport processes above  $\eta_\theta$ , but the underlying  $\eta$  surfaces nearest the interface isentropic surface  $\eta_\theta$  are correspondingly displaced upward with cold air advection and downward with warm air advection. These displacements, being intrinsically linked to isentropically amplifying baroclinic waves and the passage of cold and warm air masses, minimize vertical truncation errors in mid- to upper-tropospheric regions of maximum vertical motion relative to sigma coordinates.

### c. Vertical mass flux

In the isentropic domain of the model, the vertical mass flux through isentropic levels,  $\rho J_\theta \theta$ , is specified through a combination of (6) and model-predicted  $\rho J_\theta$ . Below  $\eta_\theta$  the vertical mass flux through model level  $\eta$  is obtained by indefinite vertical integration of the mass continuity equation (1):

$$\rho J \dot{\eta} = - \int_{\eta_s}^{\eta} \nabla_\eta \cdot (\rho J_\eta \mathbf{U}) d\eta + \frac{\partial p}{\partial t} - \frac{\partial p_s}{\partial t}. \quad (14)$$

From (10), in the lower domain between  $\eta_s$  and  $\eta_\sigma$

$$\partial p / \partial t = [1 - (\eta - \eta_s) / \eta_s] (\partial p_s / \partial t). \quad (15)$$

Substituting (15) into (14) yields the following expression for vertical mass flux in the lower domain ( $\eta_s \leq \eta \leq \eta_\sigma$ ):

$$\rho J_\eta \dot{\eta} = - \int_{\eta_s}^{\eta} \nabla_\eta \cdot (\rho J_\eta \mathbf{U}) d\eta - \frac{\partial p_s}{\partial t} \left( \frac{\eta_s - \eta}{\eta_s} \right). \quad (16)$$

For the transition domain, adding and subtracting the pressure tendency at  $\eta_\sigma$  in (14) yields

$$\begin{aligned} \rho J_\eta \dot{\eta} = & - \int_{\eta_s}^{\eta} \nabla_\eta \cdot (\rho J_\eta \mathbf{U}) d\eta + \frac{\partial p}{\partial t} - \frac{\partial p_{\eta_\sigma}}{\partial t} \\ & + \left( \frac{\partial p_{\eta_\sigma}}{\partial t} - \frac{\partial p_s}{\partial t} \right). \end{aligned} \quad (17)$$

Using (12), the tendency of pressure on model level  $\eta$  in the transition domain is given by

$$\frac{\partial p}{\partial t} = \frac{\partial p_{\eta_\sigma}}{\partial t} + \left( \frac{\partial p_\theta}{\partial t} - \frac{\partial p_{\eta_\sigma}}{\partial t} \right) \left( \frac{\eta - \eta_\sigma}{\eta_\theta - \eta_\sigma} \right). \quad (18)$$

Substitution of (18) into (17) yields an expression for vertical mass flux in the transition domain ( $\eta_\sigma \leq \eta \leq \eta_\theta$ ):

$$\begin{aligned} \rho J_\eta \dot{\eta} = & - \int_{\eta_s}^{\eta} \nabla_\eta \cdot (\rho J_\eta \mathbf{U}) d\eta + \left( \frac{\eta - \eta_\sigma}{\eta_\theta - \eta_\sigma} \right) \left( \frac{\partial p_\theta}{\partial t} - \frac{\partial p_{\eta_\sigma}}{\partial t} \right) \\ & + \left( \frac{\partial p_{\eta_\sigma}}{\partial t} - \frac{\partial p_s}{\partial t} \right). \end{aligned} \quad (19)$$

In the preceding equations, the mass flux at the top of the model and the earth's surface is assumed to vanish, and

$$\frac{\partial p_s}{\partial t} = - \int_{\eta_s}^{\eta_r} \nabla_\eta \cdot (\rho J_\eta \mathbf{U}) d\eta. \quad (20)$$

#### d. Numerics, diffusion, and parameterizations

The UW  $\theta$ - $\eta$  model employs the Arakawa A grid in combination with flux form piecewise parabolic method (PPM) numerics (Colella and Woodward 1984; Carpenter et al. 1990). The use of the A-grid was carried forward from the UW  $\theta$ - $\sigma$  model to speed development and facilitate the implementation of the flux from PPM numerics. PPM numerics provide highly accurate advection both in the vicinity of sharp gradients and smooth flows (Carpenter et al. 1990) while the monotonicity constraint employed frees the solutions from spurious oscillations, and fields such as water vapor and mass remain positive definite during integration.

The time integration was carried out with an explicit forward-backward scheme (Mesinger and Arakawa 1976) with a dynamics time step of 7.5 min for the climate simulation in section 3. Physics were called every 30 min. Fourier filtering was applied each time step

to the tendencies of the prognostic fields poleward of  $60^\circ$  in each hemisphere to suppress computational instability and preclude an undesirable restriction on the time step. The filter coefficients were determined following Suarez and Takacs (1994).

In order to control high wavenumber noise, an implicit formulation of fourth-order diffusion (Li et al. 1994) was applied to specific humidity throughout the model domain, mass in the isentropic domain, and potential temperature in the surface and transition domains. The diffusion coefficient of  $8 \times 10^{15} \text{ m}^4 \text{ s}^{-1}$  was applied globally to these fields. The zonal and meridional components of the wind were treated in the following manner. Vorticity ( $\zeta$ ) and divergence ( $\delta$ ) were calculated throughout the model domain and fourth-order diffusion was applied to these fields. Velocity potential and streamfunctions were obtained from  $\zeta$  and  $\delta$  by solving the Poisson equation using fast Fourier transforms in longitude and a finite-difference solver for the second-order differential equations in latitude (Li et al. 1994). Zonal and meridional wind components were then determined from the derivatives of the velocity potential and streamfunctions. The diffusion coefficient ( $k$ ) for  $\zeta$  and  $\delta$  was held constant on each model surface. However, since stronger undesirable noise builds in the upper troposphere and stratosphere during integration the coefficient increased in the vertical. The diffusion coefficient  $k$  increased linearly as a function of the area-averaged value of  $[1 - (p/p_s)]$  from its minimum value of  $8 \times 10^{15} \text{ m}^4 \text{ s}^{-1}$  at the earth's surface. Once the maximum value of  $3 \times 10^{16} \text{ m}^4 \text{ s}^{-1}$  was reached, the diffusion coefficient was held constant. Diffusion was applied every other model time step.

Diffusion introduced a few minimal negative values of specific humidity at each application. Negative values were removed through global borrowing following Rood's (1987) scheme described in Reames and Zapotocny (1999a). In extended integrations the mass within an isentropic layer may also become very small or negative at a limited number of grid points. If the hydrostatic pressure increment fell below 1.5 hPa at a grid point, the pressure increment was readjusted to this value employing global borrowing to ensure global mass conservation in a manner analogous to that described earlier for specific humidity.

The UW  $\theta$ - $\eta$  model incorporates the full suite of NCAR's CCM3 physical parameterizations including radiation, moist convection, vertical diffusion, gravity wave drag, PBL scheme, surface fluxes, etc. The CCM3 land surface model and multitasking capabilities have also been incorporated into the UW  $\theta$ - $\eta$  model. These physical parameterizations provide estimates of  $F_u$ ,  $F_v$ ,  $F_q$ ,  $\dot{q}$ , and  $\dot{\theta}$  for (1) through (6). Kiehl et al. (1996, 1998) provide a detailed description of the physical parameterizations employed in CCM3.

For the climate simulation in section 3, the physical parameterizations were applied using the CCM3 default settings with one exception. The relative humidity

thresholds for the calculation of cloud fraction were increased from the CCM3 threshold values of 90% for formation of high, middle, and low-level clouds, to 99% for high- and middle-level clouds, and 97% for low clouds. These changes improved the simulation of globally averaged outgoing longwave radiation (OLR) and cloudiness, and the distribution of precipitation over tropical landmasses.

### 3. A UW $\theta$ - $\eta$ climate simulation

A key objective of this study is to demonstrate the credibility of the UW  $\theta$ - $\eta$  model results from a 14-yr climate simulation. Results from two numerical experiments designed to examine the accuracy of the UW  $\theta$ - $\eta$  model numerics in simulating transport and reversible moist isentropic processes are also presented in the appendix. These experiments, following the methodology of Johnson et al. (2000, 2002), document the exceptional capabilities of the UW  $\theta$ - $\eta$  model to conserve moist entropy and potential vorticity over a 10-day period corresponding to the global water vapor residence time.

The initial data provided by the National Centers for Environmental Prediction (NCEP) Global Data Assimilation System for the 14-yr climate simulation were from 0000 UTC 15 December 1998. The data available at T126 spectral resolution on 28 vertical levels were first spectrally truncated to T42 and then linearly interpolated to a  $2.8125^\circ$  latitude-longitude grid. Next the data were vertically interpolated to UW  $\theta$ - $\eta$  model surfaces linearly with respect to pressure. The vertical structure of the UW  $\theta$ - $\eta$  model consisted of 28 layers. There were 14 isentropic layers above 336 K. Below 336 K there were 13  $\eta$  layers for the transition domain and 1  $\sigma$  layer in the surface domain (see Fig. 2). For this simulation the pressure at the upper boundary ( $\theta_T = 3300$  K) was assumed to be a uniform value of 0.1 hPa.

The appropriate specification of the upper boundary of models remains an unresolved problem. Various methods, such as the radiation boundary condition (Klemp and Duran 1983) and absorbing boundary condition, have been applied in an attempt to reduce the false reflection of vertically propagating waves from the model top. The current model does not employ an explicit treatment to control the reflection of waves at the model top. The impact on the resulting climate simulation is unknown. However, no detrimental affects were noted for the scales under consideration. Research continues to investigate the impact of the upper boundary.

The model was integrated for 14 plus years using the Atmospheric Model Intercomparison Project (AMIP) II SSTs (Taylor et al. 2001) from 15 December 1980 to March 1995. Allowing 1 yr of integration for the simulated results to be independent of the initial state, the analyses that follow focus on 13-yr seasonal means for December–January–February (DJF) and June–July–Au-

gust (JJA) unless stated otherwise. This period corresponds with the period of the first NCEP–NCAR climate reanalysis assimilated dataset (Kalnay et al. 1996), which is a primary source of validation.

The NCEP–NCAR reanalysis dataset (Kalnay et al. 1996) provides time-averaged monthly means (1982–94) for the surface and selected fields on 17 isobaric levels at  $2.5^\circ \times 2.5^\circ$  horizontal resolution. Model-simulated precipitation is compared against estimates from the Xie and Arkin (1997) analyses for the period 1979–99. The Xie and Arkin dataset is a 19-yr, global  $2.5^\circ \times 2.5^\circ$  gridded precipitation dataset derived from a combination of estimates from rain gauges, satellites, and the NCEP–NCAR reanalysis. Model precipitable water is compared with estimates from the National Aeronautics and Space Administration (NASA) Water Vapor Project (NVAP; Randel et al. 1996). This global dataset, covering the period of 1988–97, was made from a combination of retrievals from the Special Sensor Microwave Imager (SSM/I), the Television Infrared Observation Satellite (TIROS-N) Operational Vertical Sounder (TOVS), and radiosonde observations. Top-of-the-atmosphere fluxes from the Earth Radiation Budget Experiment (ERBE) are also used for validation of the UW model.

Several comparisons will be made between corresponding distributions from the UW  $\theta$ - $\eta$  model and the NCAR CCM3. As discussed in section 2d, the UW  $\theta$ - $\eta$  model employed the CCM3 physical parameterization package with only minor modifications. Such comparisons will provide insight on the impact of the UW  $\theta$ - $\eta$  model structure and dynamical core.

#### a. Mean sea level pressure

The model-simulated DJF and JJA mean sea level pressure (SLP) distributions are shown in Figs. 3a and 3b, respectively. Differences from the NCEP–NCAR reanalysis climatology (UW – NCEP–NCAR) for DJF and JJA are shown in Figs. 3c and 3d, respectively.

In both seasons the model distributions portray a realistic simulation of the observed surface circulation. The spatial patterns of the DJF Aleutian and Icelandic low pressure systems agree well with the NCEP–NCAR reanalysis data. The central pressures of both low pressure systems are within 3 hPa of the four-dimensional data assimilation (4DDA) analyses. Both the spatial patterns and magnitude of the high pressure systems over Asia and North America also agree very well with the 4DDA data with biases of less than 3 hPa over North America and eastern Asia. Throughout tropical and subtropical latitudes, the SLP is within 1–3 hPa of the NCEP–NCAR reanalysis.

The DJF SLP of the simulated Aleutian low over the eastern North Pacific is too high with maximum biases of 7–9 hPa. Erroneous low pressure extends across northern Europe into Asia with the largest differences of –7 to –9 hPa near the Caspian Sea. At NH high-

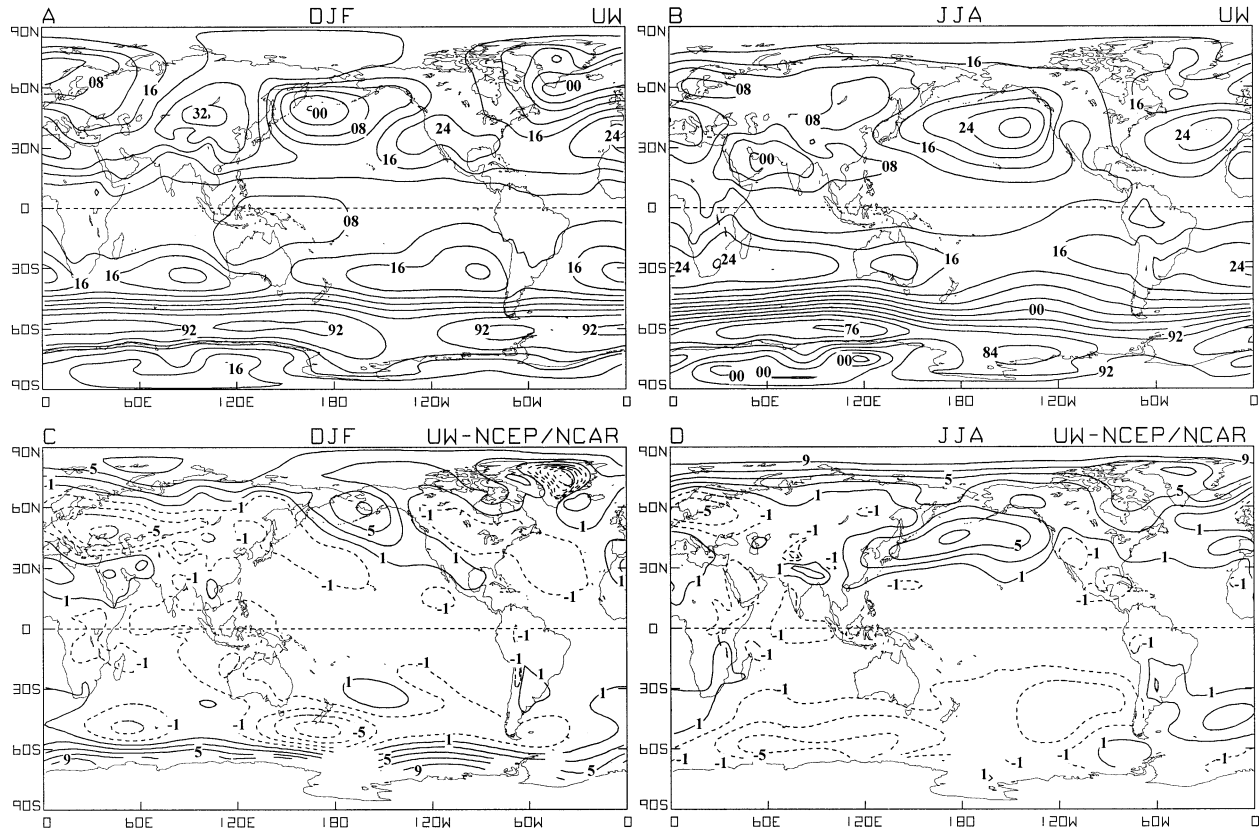


FIG. 3. The time-averaged mean sea level pressure distributions from the 13-yr UW  $\theta$ - $\eta$  model climate simulation for (a) DJF and (b) JJA as well as differences from the NCEP-NCAR reanalysis climatology (UW - NCEP-NCAR) for (c) DJF and (d) JJA. (a), (b) The contour interval is 4 hPa. Differences are contoured every 2 hPa from  $\pm 1$  hPa to identify the larger deviations from minimal deviations about 0.

latitude pressures are also too high with maximum biases of 7–9 hPa north of Asia.

In the SH, the simulated anticyclonic circulations over the eastern oceans agree well in both position and intensity with observations (see Figs. 3a,c). The DJF circumpolar trough of the SH is well defined, with minimum pressure 4–5 hPa higher than observed. The circumpolar trough is displaced  $5^{\circ}$ – $7^{\circ}$  equatorward from observed. This combination leads to negative (positive) biases over all longitudes just equatorward (poleward) of  $55^{\circ}$ S. Maximum positive biases of 7–9 hPa occur just off the coast of Antarctica. Negative biases are small except south of New Zealand where biases of  $-7$  to  $-9$  hPa are located (Fig. 3c).

In JJA (Figs. 3b,d), the salient features of the surface circulation are well simulated. The NH subtropical anticyclone over the North Pacific is stronger than observed with pressures 5–7 hPa too high over much of the extratropical North Pacific. The subtropical anticyclone over the North Atlantic is properly positioned with pressures 1–3 hPa higher than observed. As was observed in DJF, pressures over NH high latitudes are too high with values 9–11 hPa too high at the North Pole. Reasons for the persistent anomalous high pres-

sure over NH high latitudes are currently under investigation.

The JJA SLP distribution in SH subtropics is well simulated with slightly lower pressures than observed over the Pacific. The position of the simulated SH circumpolar trough agrees very well with the NCEP-NCAR climatology. The simulated SLP is 5–7 hPa too low off the coast of Antarctica between  $50^{\circ}$  and  $140^{\circ}$ E (Fig. 3d), 3–5 hPa too low over a portion of the eastern South Pacific, and 3–5 hPa too high over middle latitude portions of the South Atlantic Ocean.

## b. Geopotential height fields

### 1) 500-hPa HEIGHTS

Figure 4 shows the 13-yr mean 500-hPa geopotential height fields for DJF (Fig. 4a) and JJA (Fig. 4b) from the UW  $\theta$ - $\eta$  model. The corresponding difference fields (UW - NCEP-NCAR) are displayed in Figs. 4c and 4d, respectively.

In DJF, the model captures the major NH troughs over the east coasts of Asia and North America as well as the weaker trough over eastern Europe. The NH ridges

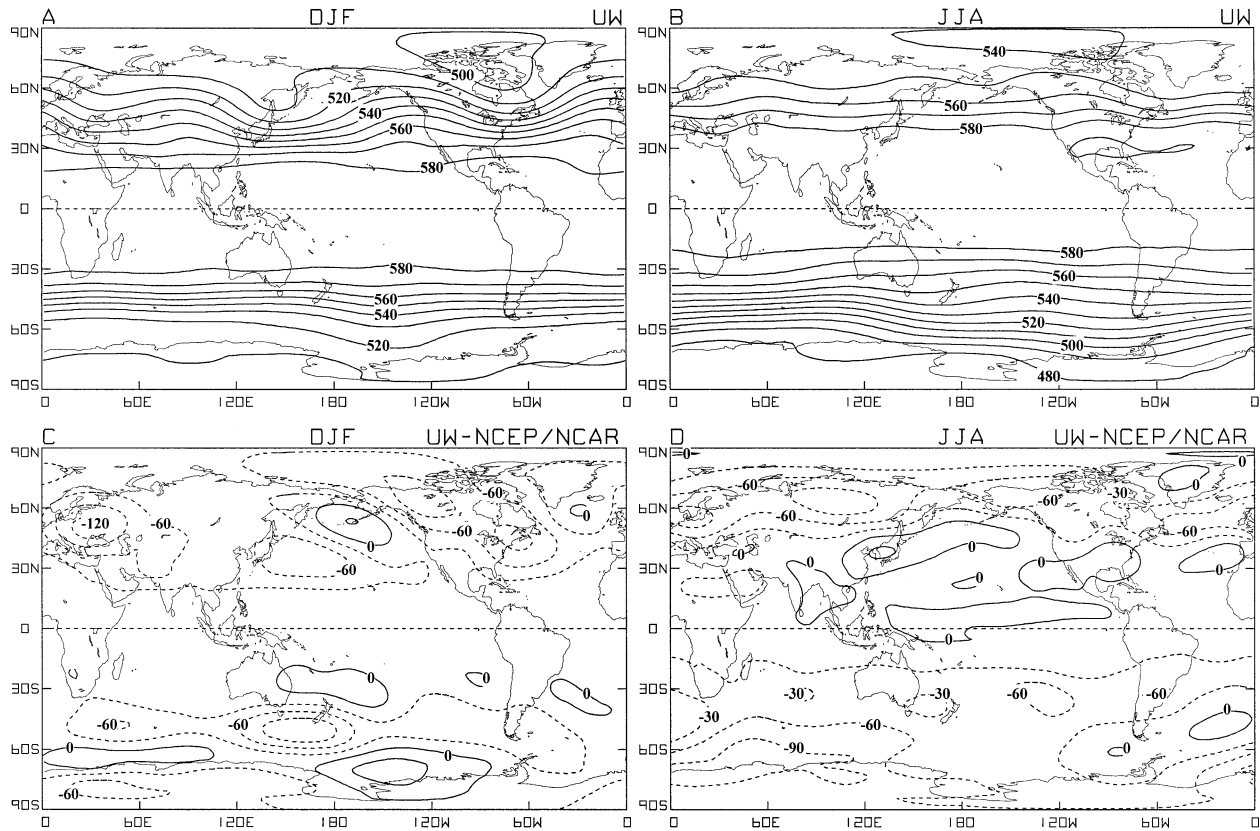


FIG. 4. The time-averaged 500-hPa geopotential height distributions from the 13-yr UW  $\theta$ - $\eta$  model climate simulation for (a) DJF and (b) JJA as well as differences from the NCEP-NCAR reanalysis climatology (UW - NCEP-NCAR) for (c) DJF and (d) JJA. (a), (b) The contour interval is 60 gpm. Differences are contoured every 30 gpm.

over the eastern North Pacific, western Atlantic, and eastern Asia are also well simulated. As observed, in the SH the strongest gradient of geopotential height is confined between  $40^{\circ}$  and  $60^{\circ}$ S.

In JJA, the UW  $\theta$ - $\eta$  distribution agrees favorably with the NCEP-NCAR reanalysis. The most prominent features of the global distribution are the substantial increase of the geopotential height gradient over much of the SH relative to the DJF distribution, and the concurrent weakening of the geopotential height gradient and the meridional flow over the NH (Fig. 4b).

The UW - NCEP-NCAR difference fields for DJF and JJA (Figs. 4c,d) show that simulated 500-hPa heights are at least 30 m too low over much of the extratropical latitudes in each season indicative of a low-to-middle troposphere cold bias (see Fig. 8). Maximum negative biases of  $-90$  to  $-120$  m are found over regions of Europe, Canada, the western North Atlantic and south of New Zealand in DJF (Fig. 4c), and over Eurasia and SH high latitudes between  $0^{\circ}$  and  $120^{\circ}$ E in JJA (Fig. 4d).

## 2) 200-HPA GEOPOTENTIAL HEIGHT ZONAL ANOMALIES

In order to further understand the UW  $\theta$ - $\eta$  model's capability to simulate the time-averaged longwave struc-

ture, the zonal means have been removed from the 200-hPa time-averaged geopotential height fields. Figure 5 shows the geopotential height zonal anomalies at 200 hPa for DJF (Fig. 5a) and JJA (Fig. 5b) from the UW  $\theta$ - $\eta$  model. Corresponding distributions from the NCEP-NCAR reanalysis are shown in Figs. 5c and 5d, respectively.

In DJF (Figs. 5a,c), both the UW model simulation and the NCEP-NCAR reanalysis show a dominant wavenumber-2 (1) pattern in the NH (SH) extratropics. The anomaly patterns are also similar in tropical/subtropical latitudes. The comparison shows relatively close correspondence in both the position and intensity of the major troughs and ridges over most regions with largest differences associated with a slightly different tilt of the ridge-trough system over North America, and over the South Pacific extratropics south and east of Australia.

In JJA, comparison again shows that the UW  $\theta$ - $\eta$  model replicates the pattern of the NCEP-NCAR reanalysis. In the SH, the UW  $\theta$ - $\eta$  model captures the wavenumber-1 pattern in both high latitudes and subtropical latitudes and the phase shift between the two regions indicated by the NCEP-NCAR reanalysis. The UW  $\theta$ - $\eta$  model overestimates the intensity of the SH

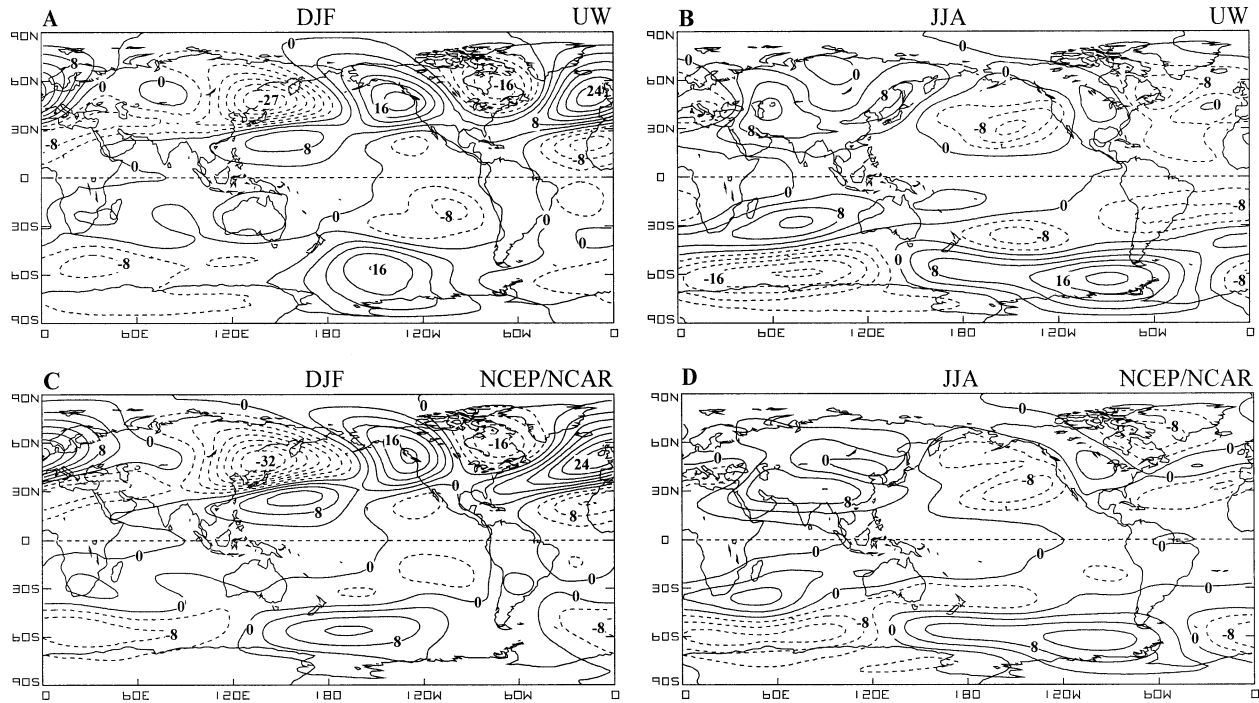


FIG. 5. Zonal geopotential height anomalies (m) at 200 hPa for DJF from the (a) UW  $\theta$ - $\eta$  model, and (c) NCEP-NCAR reanalysis, and for JJA from the (b) UW  $\theta$ - $\eta$  model, and (d) NCEP-NCAR reanalysis.

anomalies in both high and subtropical latitudes indicating larger-amplitude time-averaged waves in the model. In the NH, the largest differences from the NCEP-NCAR reanalysis occur along the east coast of Asia and over the North Atlantic east of Canada, where the UW  $\theta$ - $\eta$  model overestimates the amplitude of the trough in this region.

### c. Precipitation

The model-simulated DJF and JJA season-averaged precipitation (Figs. 6a and 6b) is compared with corresponding estimates for 1979-99 from Xie and Arkin (1997; Figs. 6c and 6d). Considering the different time periods and the uncertainty that must be assigned to the observed distributions, the simulated and observed distributions agree favorably.

Both the simulated and observed DJF distributions show the largest precipitation amounts over tropical landmasses, and along the ITCZ and South Pacific convergence zone (SPCZ). In general the model-simulated precipitation is slightly larger than observed in tropical latitudes, particularly over the landmasses. The north-south extent of the simulated precipitation is larger than observed over the Indian Ocean and western Pacific Ocean. A large localized maximum west of Mexico near 12°N in the simulated precipitation has no counterpart in the observed distribution.

The positioning of the maxima and the orientation of the axes of maximum precipitation along the North Pa-

cific and North Atlantic oceanic cyclone tracks agree well with observations. In both basins, the magnitude of precipitation is close to observed with the maximum in the North Pacific being larger than in the Xie and Arkin climatology.

The simulated DJF zonally averaged precipitation agrees closely with the Xie and Arkin distribution (Fig. 7a). In particular the model properly captures the magnitude of the two observed tropical maxima, one just poleward of the equator in each hemisphere. In both distributions, the SH maximum is largest although the model maxima are displaced slightly south of observed. This tropical distribution agrees much better with observational estimates than the corresponding distribution from CCM3, where the tropical maximum lies in the NH (Hack et al. 1998). The UW model resolves the secondary precipitation maxima in the middle latitudes of both hemispheres, although with increased magnitude. The model depicts a broader region of low-latitude precipitation and a slight poleward shift of the subtropical minima relative to the Xie and Arkin climatology. A similar tendency occurs in many of the models analyzed for AMIP (Gates et al. 1999).

In JJA the spatial distribution of precipitation associated with the monsoonal circulations over Africa, Southeast Asia, and the Americas is well simulated by the UW  $\theta$ - $\eta$  model. Both the model (Fig. 6b) and observed (Fig. 6d) distributions show a well-defined ITCZ just north of the equator over the Pacific and Atlantic Oceans, Africa, and South America. A broad region of

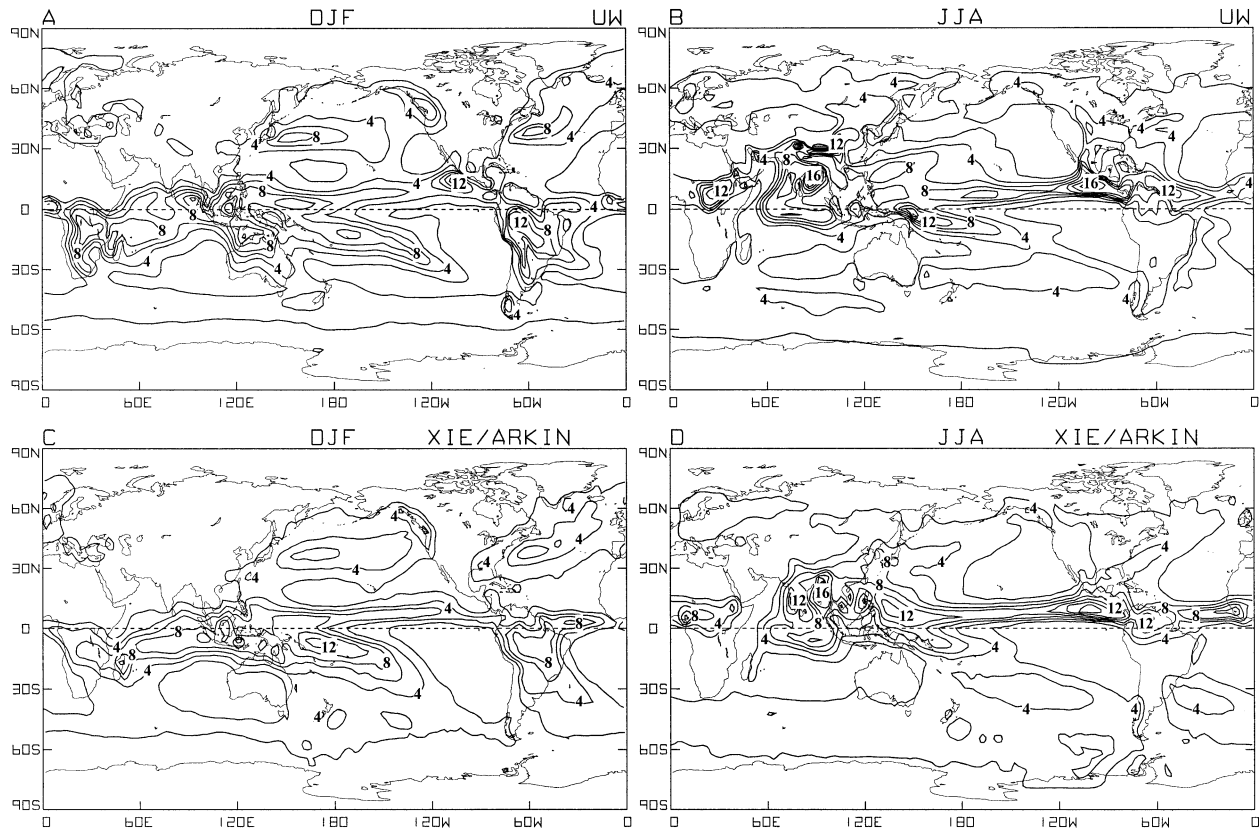


FIG. 6. The time-averaged distributions of precipitation ( $\text{mm day}^{-1}$ ) from the 13-yr UW  $\theta$ - $\eta$  model climate simulation for (a) DJF and (b) JJA and from the Xie and Arkin precipitation climatology for 1979–99 for (c) DJF and (d) JJA.

precipitation extends across Southeast Asia, the Indian Ocean, and the western Pacific Ocean associated with the summer Asian monsoon. The simulated maximum precipitation is properly located over the northern Bay of Bengal. In general the UW  $\theta$ - $\eta$  model overestimates precipitation over the NH Indian Ocean and underestimates the precipitation over the eastern portion of the southeast monsoon region. This bias pattern is also evident in CCM3 (Fig. 27 of Hurrell et al. 1998). The monsoon precipitation over Central America is well simulated although the UW  $\theta$ - $\eta$  model oversimulates precipitation to the north over Mexico and the western United States.

The meridional structure of the JJA zonally averaged precipitation is well resolved over all latitudes. In JJA (Fig. 7b) the simulated tropical maximum near  $10^{\circ}\text{N}$  agrees closely with the observed value in both magnitude and position. CCM3 also captures the location of the tropical maximum (Hack et al. 1998) but the magnitude is  $1$ – $1.5 \text{ mm day}^{-1}$  less than observed. The model depicts slightly more precipitation than observed over nearly all latitudes with the maximum differences between  $40^{\circ}$  and  $60^{\circ}$  in each hemisphere. Similar to the DJF distribution (Fig. 7a), the simulated distribution has

a broader region of tropical precipitation relative to climatology.

Figure 8 provides a measure of the UW  $\theta$ - $\eta$  model's capability to respond to anomalous SST forcing by displaying the difference between seasonally averaged precipitation during ENSO warm and cold events. Figure 8 shows the observed (Fig. 8a) and simulated (Fig. 8b) DJF 1987/88 (warm event) minus DJF 1988/89 (cold event) precipitation difference fields. Both fields depict a large positive maximum centered on the equator near the date line associated with the anomalous precipitation during the DJF 1987/88 warm event. Axes of positive differences extend north of the equator into the eastern North Pacific and southeastward along the SPCZ. In both distributions, negative values with comparable magnitudes surround this major anomaly on the north, south, and much of the west. A narrow tongue of positive values extends from the major anomaly westward just north of the equator into the Indian Ocean in the simulated distribution. The observed distribution indicates small negative values with isolated positive values in the corresponding area. Overall the magnitude and spatial distribution of differences agree well between the simulated and observed fields. This comparison

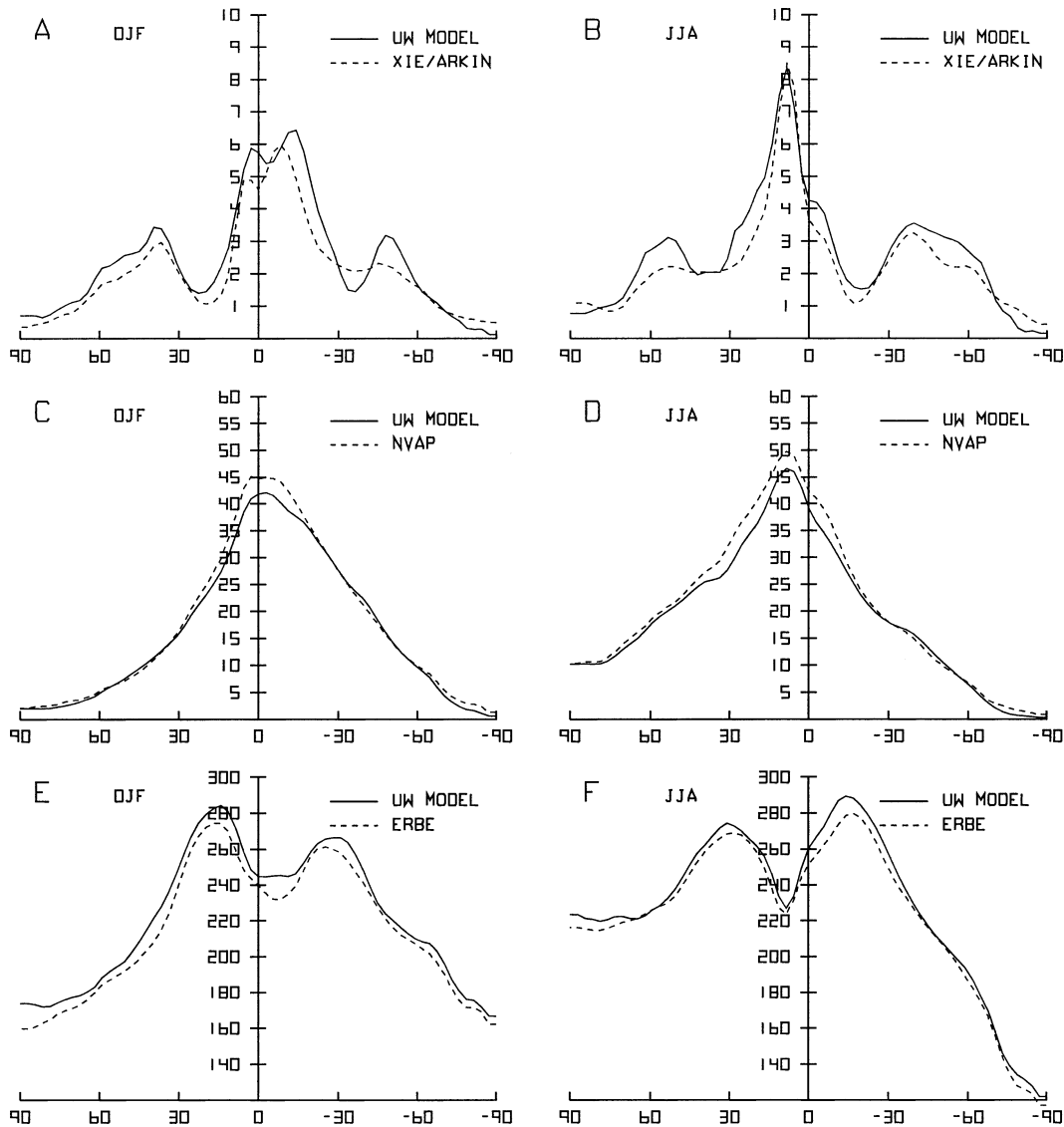


FIG. 7. Temporally and zonally averaged fields (solid lines) from the 13-yr UW  $\theta$ - $\eta$  model climate simulation and observations (dashed lines) of (a) precipitation ( $\text{mm day}^{-1}$ ), (c) precipitable water (mm), (e) and OLR ( $\text{W m}^{-2}$ ) for DJF and (b), (d), and (f) for JJA. The observations are from the (a), (b) Xie and Arkin (1997) precipitation climatology for 1979–99; (c), (d) NVAP analyses for 1988–97; and (e), (f) ERBE data for 1986–89.

demonstrates the capability of the model to respond realistically to anomalous SST forcing.

#### d. Zonally averaged distributions

For the following, temperature and the zonal component of the wind have been interpolated vertically from UW  $\theta$ - $\eta$  model surfaces to the pressure levels used in the NCEP–NCAR reanalysis archive, assuming a linear variation with pressure. The NCEP–NCAR data were linearly interpolated in latitude and longitude to the horizontal grid of the UW  $\theta$ - $\eta$  model.

Figure 9 shows the zonally averaged temperature for DJF (Fig. 9a) and JJA (Fig. 9b) from the UW  $\theta$ - $\eta$  model.

Difference fields (UW – NCEP–NCAR) are shown in Figs. 9c and 9d, respectively. The UW  $\theta$ - $\eta$  model properly simulates the structure and seasonal evolution of observed zonally averaged temperature. In DJF, simulated temperatures are within 3 K of the NCEP–NCAR reanalysis values between 30°N and 40°S. North of 30°N, simulated temperatures are 2–5 K too cold below 300 hPa and 6–7 K too cold at the surface poleward of 70°N. Between 90°N and 50°S, simulated temperatures are within 3 K of the NCEP–NCAR reanalysis above 250 hPa except at 40°N near 200 hPa where a 4–5 K warm bias is indicated. In the SH, a cold bias spans much of the atmosphere south of 40°S. Maximum biases of –10 to –11 K occur near 250 hPa at 70°S.

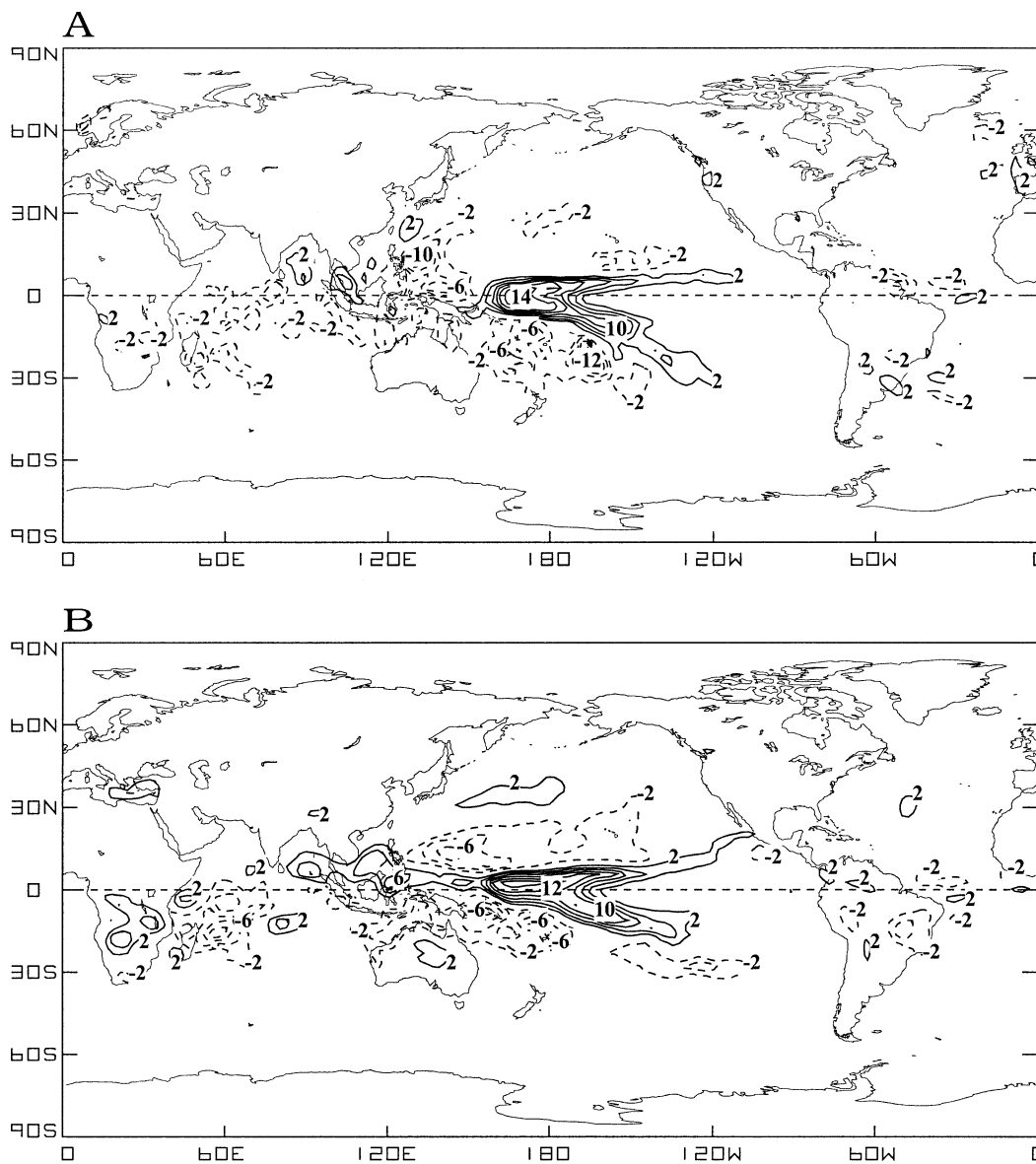


FIG. 8. Global distributions of the difference (DJF 1987/88 – DJF 1988/89) between seasonally averaged precipitation for DJF 1987/88 and DJF 1988/89 ( $\text{mm day}^{-1}$ ) from the (a) Xie and Arkin (1997) climatology and (b) UW  $\theta$ - $\eta$  model climate simulation.

In JJA, biases are less than 2 K between 30°S and 45°N except near 150 hPa at the equator where a cold bias of  $-2$  to  $-3$  K is indicated. In the NH, simulated temperatures are 4–7 K too cold throughout the lower and middle troposphere poleward of 55°N. At these same latitudes, the bias ranges between  $\pm 2$  K above 200 hPa. In the SH poleward of 45°S, simulated temperatures are 2–7 K colder than observed through the atmosphere. Maximum SH biases of  $-6$  to  $-7$  K occur poleward of 50°S centered near 225 hPa.

Cold biases in the high troposphere and lower stratosphere of polar regions have been a long-standing problem in climate model simulations (Boer et al. 1991,

1992; Johnson 1997). Reasons for this pervasive cold bias remain elusive. Deficient model physics and insufficient vertical resolution may play important roles, as well as errors in models' advection schemes (Gates et al. 1999; Hack et al. 1998). The large differences in the orientation of the potential temperature and sigma surfaces in the upper troposphere and lower stratosphere of SH middle and high latitudes in the cross section in Fig. 2 clearly demonstrate the three-dimensional complexity involved in resolving isentropic transport processes within sigma coordinate models in these regions.

In comparison of CCM3 and the NCEP–NCAR reanalysis, Hack et al. (1998) show a DJF cold bias in

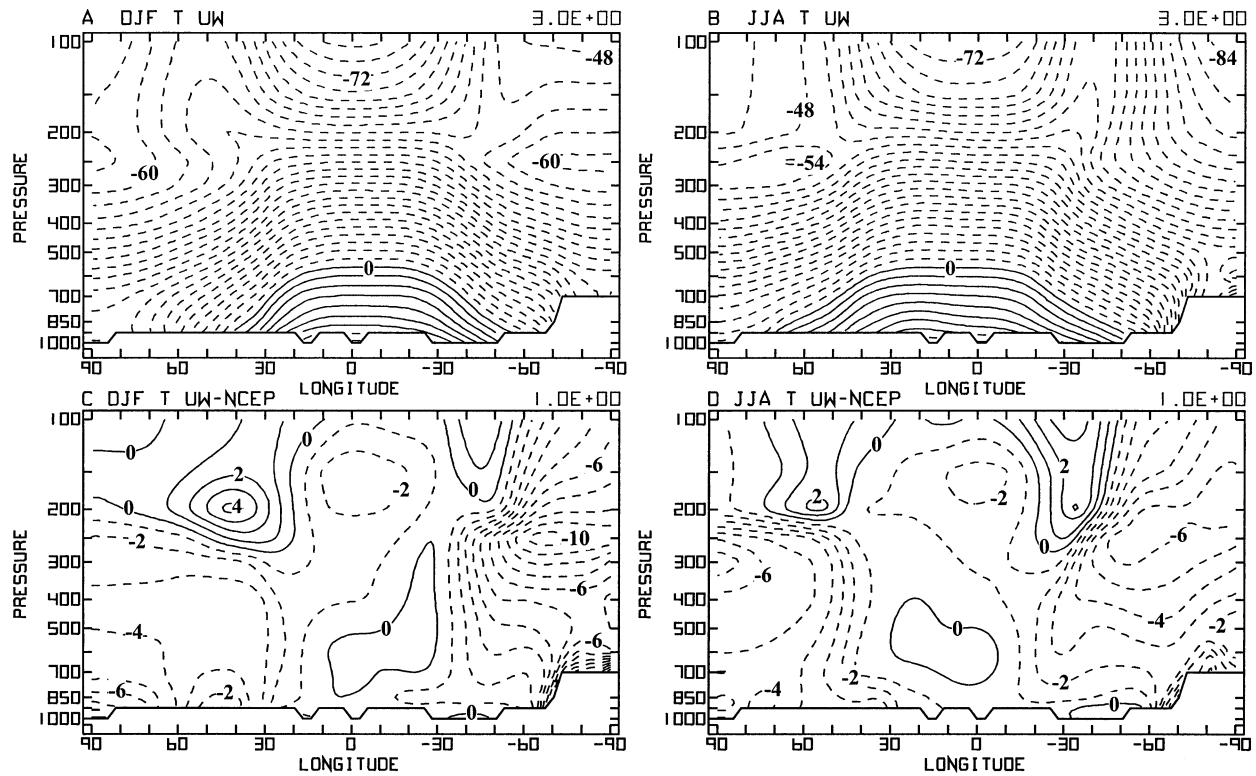


FIG. 9. Zonally and seasonally averaged distributions of UW  $\theta$ - $\eta$  model simulated temperature ( $^{\circ}\text{C}$ ) from the 13-yr climate simulation for (a) DJF and (b) JJA and (c) and (d) the respective difference fields UW - NCEP-NCAR.

CCM3 of 14–15 K near 200 hPa in SH polar latitudes (see their Fig. 4). This compares to a 10–11 K cold bias at 250 hPa in the same region for the UW  $\theta$ - $\eta$  model. CCM3 has a NH maximum cold bias of 4–5 K near 200 hPa north of  $60^{\circ}\text{N}$  while the UW  $\theta$ - $\eta$  model has temperatures within +1 to  $-2$  K of the observed distribution in the same region. In portions of the high-latitude troposphere of both hemispheres, the UW  $\theta$ - $\eta$  model has a 1–3 K larger cold bias than CCM3.

In JJA, CCM3 temperatures are too cold by a maximum of  $-9$  to  $-10$  K near  $60^{\circ}\text{S}$  at 200 hPa and by  $-10$  to  $-11$  K at 200 hPa near the North Pole (see Fig. 4 of Hack et al. 1998). In comparison, the UW  $\theta$ - $\eta$  model temperatures are too cold by a maximum of  $-6$  to  $-7$  K in SH high latitudes and  $-7$  to  $-8$  K near 300 hPa in NH polar latitudes. In the middle and lower troposphere of extratropical latitudes, the UW  $\theta$ - $\eta$  model cold bias is approximately 1–2 K larger than in CCM3.

Poleward of  $60^{\circ}$  in each hemisphere the UW  $\theta$ - $\eta$  model-simulated cold bias is appreciably smaller in the upper troposphere/lower stratosphere than in CCM3 and other Eulerian sigma coordinate models in both DJF and JJA. This portion of the atmosphere is fully described by isentropic coordinates in the UW  $\theta$ - $\eta$  model. In the lower portion of the atmosphere where sigma coordinates in effect represent the atmosphere, the UW  $\theta$ - $\eta$  model cold bias is as large or larger than CCM3.

Figures 10a and 10b show the zonally averaged zonal

wind component for DJF and JJA. Figures 10c and 10d show the difference field (UW - NCEP-NCAR) for each season. In DJF, minimal differences occur poleward of  $30^{\circ}\text{N}$  and  $70^{\circ}\text{S}$  (Fig. 10c). In the NH, a maximum westerly bias of 6–8  $\text{m s}^{-1}$  occurs on the equatorward side of the jet core near 300 hPa. An easterly bias of 6–8  $\text{m s}^{-1}$  is located above 150 hPa near  $10^{\circ}\text{N}$  and  $20^{\circ}\text{S}$ . A westerly bias of greater than 4  $\text{m s}^{-1}$  spans the region between  $35^{\circ}$  and  $55^{\circ}\text{S}$  above 400 hPa, associated in part with the equatorward shift of the zonally averaged jet compared to the 4DDA data. Maximum biases of 10–12  $\text{m s}^{-1}$  are found near 200 hPa at  $40^{\circ}\text{S}$ .

The JJA distribution in Fig. 10b shows the expected increase in intensity of the SH zonal circulation and the concurrent decrease of the NH circulation relative to DJF. The SH maxima near 250 hPa is separated from the secondary maxima in the stratosphere at  $50^{\circ}\text{S}$ , although not as distinctly as observed. The simulated jet maxima (Fig. 10b) in both hemispheres are stronger than observed (Fig. 10d). Westerly biases of 4–8  $\text{m s}^{-1}$  occur above 450 hPa near  $50^{\circ}\text{N}$ , between 500 and 250 hPa from the equator to  $30^{\circ}\text{S}$  and above 250 hPa near  $40^{\circ}\text{S}$ . The maximum westerly bias is 10–12  $\text{m s}^{-1}$  near 100 hPa at  $45^{\circ}\text{S}$ .

The UW model and CCM3 display a relatively similar pattern of DJF biases poleward of  $30^{\circ}$  in each hemisphere, although differences in magnitude and location of maxima are evident. At the equator CCM3 has a

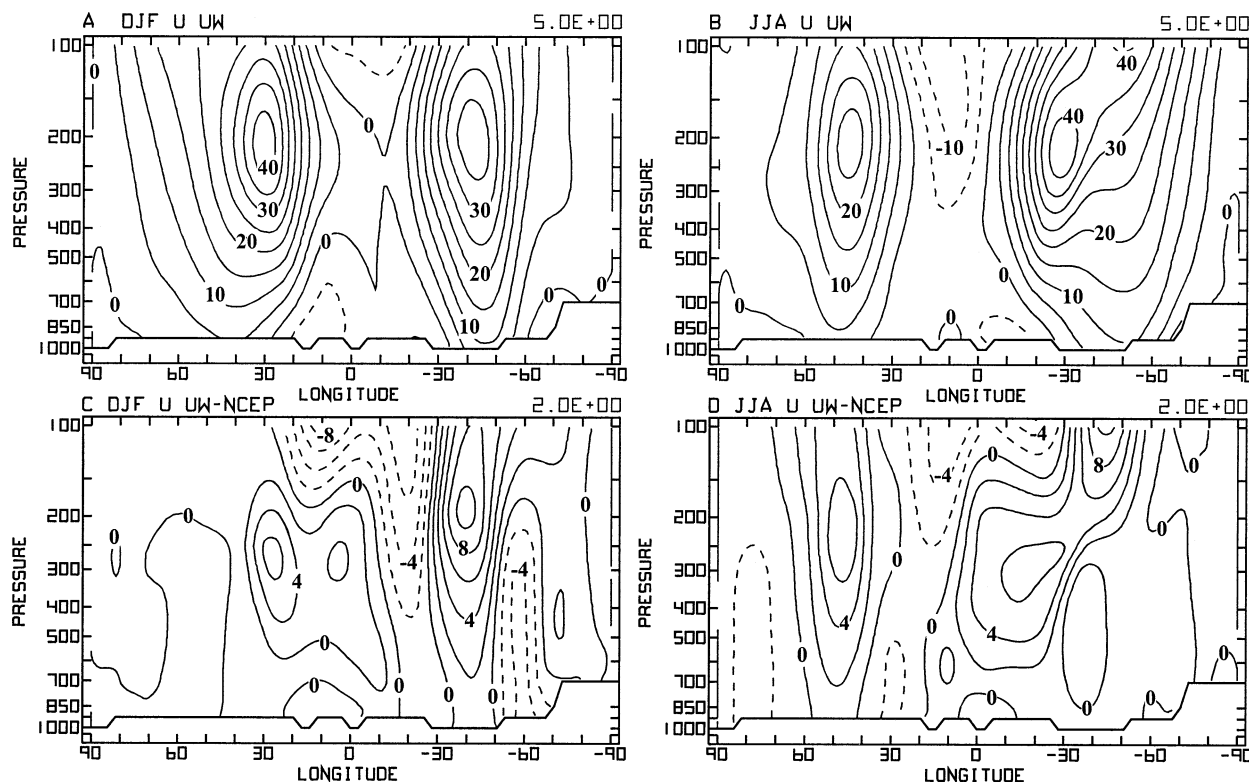


FIG. 10. Zonally and seasonally averaged distributions of the UW  $\theta$ - $\eta$  model simulated  $u$  component of the wind ( $\text{m s}^{-1}$ ) from the 13-yr climate simulation for (a) DJF and (b) JJA and (c) and (d) the difference field UW - NCEP-NCAR.

westerly bias of  $4\text{--}6 \text{ m s}^{-1}$  near 175 hPa (see Fig. 12 of Hurrell et al. 1998) compared to biases of  $\pm 2 \text{ m s}^{-1}$  at the same location in the UW model. Biases of  $-6$  to  $-8 \text{ m s}^{-1}$  above 150 hPa at  $20^\circ\text{S}$  and  $-4$  to  $-6 \text{ m s}^{-1}$  in the lower troposphere near  $60^\circ\text{S}$  in the UW model compare with biases of less than  $2 \text{ m s}^{-1}$  in the same regions in CCM3. Maximum westerly biases of  $10\text{--}12 \text{ m s}^{-1}$  in both models are located in the upper troposphere/lower stratosphere in SH middle latitudes.

The pattern of biases is also similar between the UW model and CCM3 in JJA. Largest biases in both models are found in the middle-latitude upper troposphere/low-

er stratosphere of both hemispheres. In the NH, maximum biases of  $6\text{--}8 \text{ m s}^{-1}$  in the UW model compare with biases of  $8\text{--}10 \text{ m s}^{-1}$  in CCM3. In the SH middle latitudes, maximum biases of  $8\text{--}10 \text{ m s}^{-1}$  occur in the UW model compared to  $12\text{--}14 \text{ m s}^{-1}$  in CCM3.

#### e. Global averaged results

Table 1 presents the 13-yr mean annual global averages for several fields along with observational estimates. The UW  $\theta$ - $\eta$  model values agree favorably with the “observed” values falling within the realm of uncertainty that must be assigned to these observed fields. The “all sky” and “clear sky” OLR fields are larger than estimates from ERBE by  $3.6$  and  $2.3 \text{ W m}^{-2}$ , respectively. Zonally averaged distributions for DJF and JJA (Figs. 7e and 7f) show the model slightly overestimates OLR at nearly all latitudes. Total cloud fraction falls within the range of observations. The simulated total cloud forcing is  $-13.4 \text{ W m}^{-2}$  compared to observed estimates of  $-19.0 \text{ W m}^{-2}$ . This difference results primarily from underestimation of the shortwave cloud forcing.

The UW  $\theta$ - $\eta$  model global annual averaged precipitation is  $3.1 \text{ mm day}^{-1}$ , compared to  $2.7 \text{ mm day}^{-1}$  from the Xie and Arkin (1997) climatology. Table 1 and Figs. 7c,d reveal a dry bias in the model-simulated pre-

TABLE 1. A comparison of annually averaged fields from the 13-yr UW  $\theta$ - $\eta$  model climate simulation to observed values. Observational estimates are from a summary by Hack et al. (1998).

Field	Observed	UW $\theta$ - $\eta$ model
All sky OLR ( $\text{W m}^{-2}$ )	234.8	238.4
Clear sky OLR ( $\text{W m}^{-2}$ )	264.0	266.3
Total cloud forcing ( $\text{W m}^{-2}$ )	-19.0	-13.4
Longwave cloud forcing ( $\text{W m}^{-2}$ )	29.2	27.9
Shortwave cloud forcing ( $\text{W m}^{-2}$ )	-48.2	-41.3
Total cloud fraction (%)	52.2 to 62.5	60.7
Precipitable water (mm)	24.7	22.8
Precipitation ( $\text{mm day}^{-1}$ )	2.7	3.1
Latent heat flux ( $\text{W m}^{-2}$ )	78.0	89.9
Sensible heat flux ( $\text{W m}^{-2}$ )	24.0	16.3

cipitable water compared to the NVAP analyses. In DJF the dry bias is confined to low latitudes of both hemispheres while it extends over the entire NH in JJA. The sum of the latent and sensible heat flux is close to observed, although the ratio of sensible to latent heat flux (Bowen ratio) differs from the observed.

#### 4. Summary

The purpose of this study was to demonstrate the capability of the UW  $\theta$ - $\eta$  model for extended integration. The results from the last 13 yr of a 14-yr climate simulation were presented and validated against NCEP-NCAR reanalysis 4DDA data and other observed data to demonstrate the viability of the UW  $\theta$ - $\eta$  model for long-term integration to simulate climate and climate change. The realistic results support continued development of hybrid isentropic coordinate models as a means to advance capabilities in the simulation of long-range transport in relation to the planetary nature of heat sources and sinks. Two numerical experiments presented in the appendix document the ability of UW  $\theta$ - $\eta$  model numerics to accurately simulate transport of moist entropy, potential vorticity, and reversible isentropic processes.

The time-mean structure of the atmosphere is well simulated by the UW  $\theta$ - $\eta$  model. Both the spatial distribution and seasonal variation of the mean SLP distribution agree well with the NCEP-NCAR reanalyses. Other than in NH polar latitudes, maximum regional biases are on the order of  $\pm 5$  hPa.

The UW  $\theta$ - $\eta$  model simulated realistic global seasonal distributions of precipitation. The model captured the primary features of observed distributions in both DJF and JJA including the precipitation associated with deep moist convection in tropical latitudes. In DJF, the position of the maxima and the orientation of axes of maximum precipitation along the NH wintertime oceanic storm tracks were well simulated. The seasonal shifts of the heavy precipitation both zonally and meridionally associated with the monsoon circulations over Southeast Asia and the Americas were well simulated. In the NH summer, the model underestimated (overestimated) the precipitation over the eastern (western) portion of the Southeast Asian monsoon region.

A limited test of the capability of the UW  $\theta$ - $\eta$  model to simulate a realistic response to anomalous tropical SSTs encountered during the ENSO cycle was also documented. The comparison of seasonal observed and model-simulated precipitation differences between ENSO warm and cold events over tropical latitudes showed the model closely reproduced the structure and magnitude of observed distributions. The overall comparison demonstrated the capability of the UW  $\theta$ - $\eta$  model to simulate realistically the precipitation induced by anomalous SST forcing.

A distinguishing feature of the UW  $\theta$ - $\eta$  simulation relative to most previous climate simulations (Boer et

al. 1991, 1992; Gates et al. 1999) is a reduced high-latitude zonally averaged cold bias in the high troposphere/low stratosphere. For example, the results show a near 30% reduction in the cold bias in these regions compared to CCM3 (Hack et al. 1998), the model from which the UW  $\theta$ - $\eta$  model physics have been taken. Reduced simulated cold biases in the same regions have been previously identified in other hybrid isentropic coordinate models (Zhu and Schneider 1997; Webster et al. 1999).

For this study the UW  $\theta$ - $\eta$  model used the NCAR CCM3 physical parameterization algorithms with only slight modification. The employment of the CCM3 parameterizations facilitated model development and provided the capabilities to undertake the climate simulations. However, the CCM3 physics have been tuned within an Eulerian spectral representation of model dynamics to replicate the climate state when employed in CCM3 (e.g., Kiehl et al. 1998; Hack et al. 1998). With parameterizations optimized for the UW  $\theta$ - $\eta$  model, presumably model biases will decrease, although this expectation remains to be established.

Relative to  $\sigma$  coordinates physical parameterizations of processes such as moist convection ideally need to be treated differently in a model based largely on isentropic coordinates. Currently, few physical parameterizations specifically developed for isentropic models exist other than those by Konor and Arakawa (2001). In future thrusts of modeling in isentropic coordinates physical parameterizations should be developed for and tested with isentropic coordinate models.

*Acknowledgments.* The authors gratefully acknowledge Judy Mohr for technical typing assistance. We thank Dr. Zhoujian Yuan for her work on early stages of this effort. This research was sponsored by the Department of Energy under Grants DE-FG02-92ER61439 and DE-FG02-01ER63254, and by NASA under Grant NAG5-9295. Computational support was provided by the National Energy Research Scientific Computing Center (NERSC), which is sponsored by the Department of Energy. The Cooperative Institute for Meteorological Satellite Studies (CIMSS) at the University of Wisconsin—Madison also provided computational support for this project.

#### APPENDIX

##### Assessments of Numerical Accuracy

Utilizing the concept of “pure error,” Johnson et al. (2000, 2002) set forth a statistical strategy to assess the numerical accuracy of global models to simulate transport and reversible processes within the fully developed nonlinear structure of NWP and climate models. The assessments focused on the appropriate conservation of potential vorticity under dry-adiabatic conditions and then moist entropy in relation to explicit simulation of

water vapor and cloud water/ice transport and cloud condensation/evaporation in conjunction with heating/cooling from phase changes. The strategy that ascertains numerical accuracy throughout the entire model domain statistically assigns numerical bias and random errors in relation to inconsistencies in the numerical representation of transport, thermodynamic, and hydrologic processes that develop over 10-day integrations, a period that corresponds with the global water vapor residence time (Peixoto and Oort 1992). Only a brief discussion is provided here, details of the experimental design and results from the UW  $\theta$ - $\sigma$  model are given in Zapotocny et al. (1996, 1997a,b) and Johnson et al. (2000, 2002).

For each experiment the UW  $\theta$ - $\eta$  model was initialized with 4 October 1994 assimilated data from the NASA Goddard Earth Observing System (*GEOS-1*) assimilation system (Schubert et al. 1993). The model was integrated at 2.8125° latitude–longitude horizontal resolution with a vertical resolution of 18 layers. The time step was 7.5 min.

#### a. Conservation of equivalent potential temperature ( $\theta_e$ )

Accurate simulation of the hydrologic cycle is fundamental for NWP and climate simulation. For accurate simulations of condensation and precipitation, first-order considerations demand that a model be capable of conserving  $\theta$  and  $\theta_e$  prior to the condensation process and  $\theta_e$  during the condensation/evaporation process. These constraints require that the *joint* distributions of mass, dry entropy, water vapor, and cloud water be simulated properly. If these distributions are poorly resolved relative to each other, the condensation/evaporation process will not be simulated accurately and reversibility will be compromised.

Following Johnson et al. (2000, 2002), the following experimental design ascertains the relative capabilities of the UW  $\theta$ - $\eta$  model to simulate reversible moist-adiabatic processes. The quantity  $\theta_e$  is first calculated for the initial time period directly at model grid points and then entered as the proxy for moist entropy in a transport equation and then treated as an inert trace constituent  $t\theta_e$  throughout the 10-day integration. The governing equations that collectively determine  $\theta_e$  include separate continuity equations for water vapor and cloud water that explicitly simulate cloudiness and their formation through condensation and their demise through evaporation. Latent heating/cooling from phase changes enters directly in the determination of the diabatic mass transport in the isentropic domain and as a source/sink of dry entropy in the lower and transition domains. Since precipitation is not allowed the global integral of water vapor and cloud water is conserved. All other parameterizations are suppressed. This experiment is equivalent to the fully reversible experiments of Johnson et al. (2000).

Figure A1 shows the bivariate distribution of paired

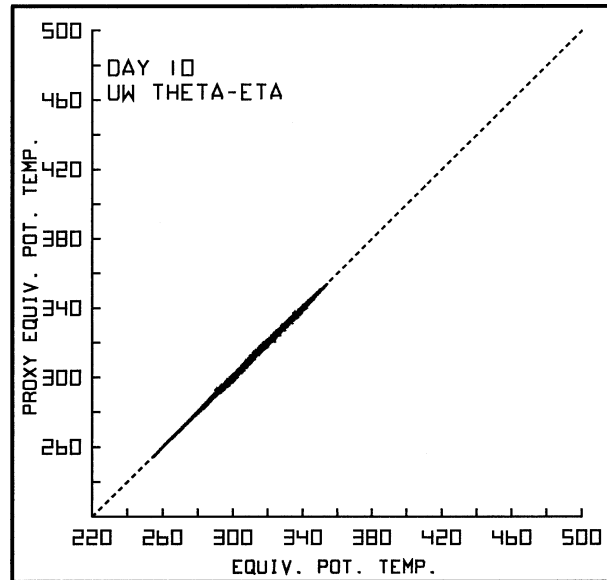


FIG. A1. The day 10 bivariate scatter distribution of equivalent potential temperature  $\theta_e$  (K) versus its proxy trace  $t\theta_e$  (K) from the UW  $\theta$ - $\eta$  model.

values of  $\theta_e$  and  $t\theta_e$  its proxy trace constituent, at day 10 for the UW  $\theta$ - $\eta$  model. Under the conditions of this experiment, appropriate conservation requires the model to preserve the initial one-to-one relationship reflected as a diagonal line extending through the origin. The minimal scatter about the diagonal at day 10 in this figure reflects the appropriate conservation of  $\theta_e$ , and the robust capabilities of the UW  $\theta$ - $\eta$  model to simulate reversible moist-adiabatic processes. The overall random component has been reduced from 0.4 K for the predecessor UW  $\theta$ - $\sigma$  model to 0.3 K for UW  $\theta$ - $\eta$  model (Johnson et al. 2000, 2002). Also the relative small bias of the pure error differences on the order of 1 K within the PBL and in isentropic layers that intersect the discrete interface of the UW  $\theta$ - $\sigma$  model has been eliminated.

#### b. Conservation of isentropic potential vorticity ( $P_\theta$ )

For accurate simulations of atmospheric circulation, a model must also be capable of appropriately conserving the joint distribution of  $P_\theta$  as a dynamic property in conjunction with atmospheric constituents including water vapor, ozone, chemical constituents, aerosols, etc. (Zapotocny et al. 1996). In this experiment the initial  $P_\theta$  distribution is computed for the initial time period at all points in the model from the state structure. This three-dimensional distribution of  $P_\theta$  is then treated as an inert trace constituent  $tP_\theta$  within a physically and dynamically consistent transport equation during the 10-day isentropic simulation.

Figure A2 shows a plot of the day 10 relationships between  $P_\theta$  and  $tP_\theta$  for each grid point in the UW  $\theta$ - $\eta$

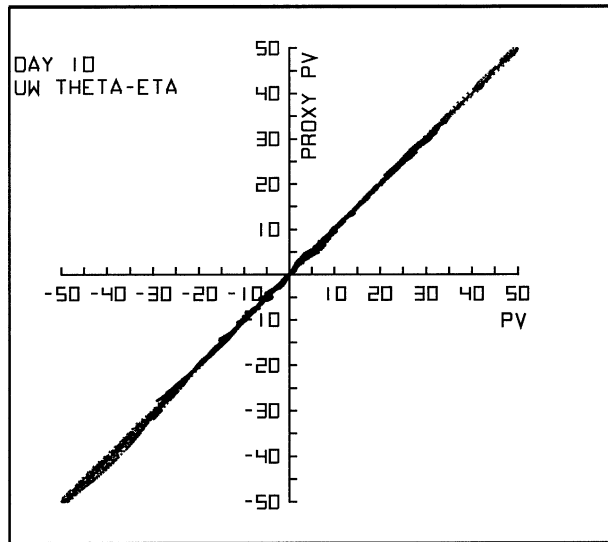


FIG. A2. The day 10 bivariate scatter distribution of isentropic potential vorticity  $P_\theta$  ( $\text{K m}^2 \text{kg}^{-1} \text{s}^{-1}$ ) vs its proxy trace  $tP_\theta$  ( $\text{K m}^2 \text{kg}^{-1} \text{s}^{-1}$ ) from the UW  $\theta$ - $\eta$  model.

model, the initial distribution of which initially determined the dashed diagonal line. Under the isentropic conditions of this experiment, this relation should be maintained throughout the 10-day integration. The results show relatively minor scatter about the diagonal at day 10 thereby documenting the high degree of conservation of  $P_\theta$  throughout the UW  $\theta$ - $\eta$  model domain. Although presented in a slightly different format, the present results are an improvement over those for the UW  $\theta$ - $\sigma$  model and markedly superior to those for the NCAR CCM2 and the UW  $\sigma$  model for the equivalent experiment shown in Fig. 2 of Zapotocny et al. (1996). Furthermore, this comparison, which includes the entire model domain as opposed to an examination of the upper troposphere and lower middle stratosphere within the  $\theta$ - $\sigma$  model, reveals that the utilization of the hybrid  $\theta$ - $\eta$  coordinate with its continuous transition removes the numerical inconsistencies that were evident in the UW  $\theta$ - $\sigma$  model PBL and lower-isentropic layers that intersected the PBL (Johnson and Yuan 1998).

#### REFERENCES

- Arakawa, A., 2000: Future development of general circulation models. *General Circulation Model Development: Past, Present and Future*, D. A. Randall, Ed., Academic Press, 721–780.
- , and V. Lamb, 1977: Computational design of the basic dynamical processes of the UCLA general circulation model. *Methods in Computational Physics*, J. Change, Ed., Vol. 17, Academic Press, 173–265.
- , and Y.-J. G. Hsu, 1990: Energy conserving and potential-entropy dissipating schemes for the shallow water equations. *Mon. Wea. Rev.*, **118**, 1960–1969.
- , and C. S. Konor, 1994: A generalized vertical coordinate and the choice of vertical grid for atmospheric models. *Proc. Int. Symp. on the Life Cycles of Extratropical Cyclones*, Vol. 3, Bergen, Norway, Amer. Meteor. Soc. and Norwegian Geophysical Society, 259–264.
- Benjamin, S. G., 1989: An isentropic meso- $\alpha$ -scale analysis system and its sensitivity to aircraft and surface observations. *Mon. Wea. Rev.*, **117**, 1586–1603.
- , G. A. Grell, J. M. Brown, R. Bleck, K. J. Brundage, T. L. Smith, and P. A. Miller, 1994: An operational isentropic/sigma hybrid forecast model and data assimilation system. *Proc. Int. Symp. on the Life Cycles of Extratropical Cyclones*, Vol. 3, Bergen, Norway, Amer. Meteor. Soc. and Norwegian Geophysical Society, 259–264.
- Bleck, R., 1978: On the use of hybrid vertical coordinates in numerical weather prediction models. *Mon. Wea. Rev.*, **106**, 1233–1244.
- , and S. G. Benjamin, 1993: Regional weather prediction with a model combining terrain-following and isentropic coordinates. Part I: Model description. *Mon. Wea. Rev.*, **121**, 1770–1785.
- Boer, G. J., and Coauthors, 1991: An intercomparison of the climates simulated by 14 atmospheric general circulation models. WCRP Rep. 58, WMO/TD-425, 165 pp.
- , and Coauthors, 1992: Some results from an intercomparison of the climates simulated by 14 atmospheric general circulation models. *J. Geophys. Res.*, **97**, 12 771–12 786.
- Carpenter, R. L., Jr., K. K. Droegemeier, P. R. Woodward, and C. E. Hane, 1990: Application of the piecewise parabolic method (PPM) to meteorological modeling. *Mon. Wea. Rev.*, **118**, 586–612.
- Chipperfield, M. P., J. A. Pyle, C. E. Blom, N. Glatthor, M. Hopfner, T. Gulde, Ch. Piesch, and P. Simon, 1995: The variability of  $\text{ClONO}_2$  in the Arctic Polar Vortex: Comparison of Transall MIPAS measurements and 3D model results. *J. Geophys. Res.*, **100**, 9115–9129.
- Colella, P., and P. R. Woodward, 1984: The piecewise parabolic method (PPM) for gas-dynamical simulations. *J. Comput. Phys.*, **54**, 174–201.
- Egger, J. A., 1999: Numerical generation of entropies. *Mon. Wea. Rev.*, **127**, 2211–2216.
- Gates, W. L., and Coauthors, 1999: An overview of the results of the Atmospheric Intercomparison Project (AMIP I). *Bull. Amer. Meteor. Soc.*, **80**, 29–55.
- Hack, J. J., J. T. Kiehl, and J. W. Hurrell, 1998: The hydrologic and thermodynamic characteristics of the NCAR CCM3. *J. Climate*, **11**, 1179–1206.
- Hsu, Y.-J. G., and A. Arakawa, 1990: Numerical modeling of the atmosphere with an isentropic vertical coordinate. *Mon. Wea. Rev.*, **118**, 1933–1959.
- Hurrell, J. W., J. J. Hack, B. A. Boville, D. L. Williamson, and J. T. Kiehl, 1998: The dynamical simulation of the NCAR Community Climate Model version 3 (CCM3). *J. Climate*, **11**, 1207–1236.
- Johnson, D. R., 1980: A generalized transport equation for use with meteorological coordinate systems. *Mon. Wea. Rev.*, **108**, 733–745.
- , 1989: The forcing and maintenance of global monsoonal circulations: An isentropic analysis. *Advances in Geophysics*, Vol. 31, Academic Press, 43–316.
- , 1997: “General coldness of climate models” and the Second Law: Implications for modeling the earth system. *J. Climate*, **10**, 2826–2846.
- , and Z. Yuan, 1998: The development and initial tests of an atmospheric model based on a vertical coordinate with a smooth transition from terrain following to isentropic coordinates. *Adv. Atmos. Sci.*, **15**, 283–299.
- , T. H. Zapotocny, F. M. Reames, B. J. Wolf, and R. B. Pierce, 1993: A comparison of simulated precipitation by hybrid isentropic-sigma and sigma models. *Mon. Wea. Rev.*, **121**, 2088–2114.
- , A. J. Lenzen, T. H. Zapotocny, and T. K. Schaack, 2000: Numerical uncertainties in the simulation of reversible isentropic processes and entropy conservation. *J. Climate*, **13**, 3860–3884.
- , A. J. Lenzen, T. H. Zapotocny, and T. K. Schaack, 2002: Nu-

- merical uncertainties in the simulation of reversible isentropic processes and entropy conservation: Part II. *J. Climate*, **15**, 1777–1804.
- Kalnay, E., and Coauthors, 1996: The NCEP/NCAR 40-Year Reanalysis Project. *Bull. Amer. Meteor. Soc.*, **77**, 437–471.
- Kiehl, J. T., J. J. Hack, G. B. Bonan, B. A. Boville, B. P. Briegleb, D. L. Williamson, and P. J. Rasch, 1996: Description of the NCAR Community Climate Model (CCM3). NCAR Tech. Note NCAR/TN-420+STR, 152 pp.
- , —, —, —, D. L. Williamson, and P. J. Rasch, 1998: The National Center for Atmospheric Research Community Climate Model: CCM3. *J. Climate*, **11**, 1131–1149.
- Klemp, J. B., and D. R. Duran, 1983: An upper boundary condition permitting internal gravity wave radiation in numerical mesoscale models. *Mon. Wea. Rev.*, **111**, 430–444.
- Konor, C. S., and A. Arakawa, 1997: Design of an atmospheric model based on a generalized vertical coordinate. *Mon. Wea. Rev.*, **125**, 1649–1673.
- , and —, 2001: Incorporation of moist processes and a PBL parameterization into the generalized vertical coordinate model. Tech. Rep. 102, Department of Atmospheric Sciences, UCLA, 63 pp.
- , C. R. Mechoso, and A. Arakawa, 1994: Comparison of frontogenesis simulations with isentropic and normalized pressure vertical coordinates. *Proc. Int. Symp. on the Life Cycles of Extratropical Cyclones*, Vol. 2, Bergen, Norway, Amer. Meteor. Soc. and Norwegian Geophysical Society, 264–268.
- Li, Y., S. Moorthi, and J. R. Bates, 1994: Direct solution of the implicit formulation of fourth order horizontal diffusion for gridpoint models on the sphere. Technical Report Series on Global Modeling and Data Assimilation, M. J. Suarez, Ed., NASA Tech. Memo. 104606, Vol. 2, 42 pp.
- Mesinger, F., and A. Arakawa, 1976: *Numerical Methods Used in Atmospheric Models*, Vol. 1. GARP Publication Series No. 17, WMO, Amer. Meteor. Soc. and Norwegian Geophysical Society, 264–268.
- Peixoto, J. P., and A. H. Oort, 1992: *Physics of Climate*. American Institute of Physics, 520 pp.
- Pierce, R. B., and T. D. A. Fairlie, 1993: Chaotic advection in the stratosphere: Implications for the dispersal of chemically perturbed air from the polar vortex. *J. Geophys. Res.*, **98D**, 18 589–18 595.
- , D. R. Johnson, F. M. Reames, T. H. Zapotocny, and B. J. Wolf, 1991: Numerical investigations with a hybrid isentropic–sigma model. Part I: Normal-mode characteristics. *J. Atmos. Sci.*, **48**, 2005–2024.
- Randel, D. L., T. H. Vonder Haar, M. A. Ringerud, G. L. Stephens, T. J. Greenwald, and C. L. Combs, 1996: A new global water vapor dataset. *Bull. Amer. Meteor. Soc.*, **77**, 1233–1246.
- Reames, F. M., and T. H. Zapotocny, 1999a: Inert trace constituent transport in sigma and hybrid isentropic–sigma models. Part I: Nine advection algorithms. *Mon. Wea. Rev.*, **127**, 173–187.
- , and —, 1999b: Inert trace constituent transport in sigma and hybrid isentropic–sigma models. Part II: Twelve semi-Lagrangian algorithms. *Mon. Wea. Rev.*, **127**, 188–200.
- Rood, R. B., 1987: Numerical advection algorithms and their role in atmospheric transport and chemistry models. *Rev. Geophys.*, **25**, 71–100.
- Schubert, S. D., R. B. Rood, and J. Pfaendtner, 1993: An assimilated dataset for earth science applications. *Bull. Amer. Meteor. Soc.*, **74**, 2331–2342.
- Suarez, M. J., and L. L. Takacs, cited 1994: Documentation of the ARIES/GEOS Dynamical Core: Version 2. [Available online at [http://nsipp.gsfc.nasa.gov/reports/volume\\_5.pdf](http://nsipp.gsfc.nasa.gov/reports/volume_5.pdf)].
- Taylor, K. E., D. Williamson, and F. Zwiers, 2001: AMIP II sea surface temperature and sea ice concentration boundary conditions. [Available online at <http://www-pcmdi.lln.gov/amip/AMIPEXPDSN/BUS/amip2bcs.html>].
- Thuburn, J., 1993: Baroclinic-wave life cycles, climate simulations and cross-isentropic mass flow in a hybrid isentropic coordinate GCM. *Quart. J. Roy. Meteor. Soc.*, **119**, 489–508.
- Webster, S., J. T. Thuburn, G. Hoskins, and M. Rodwell, 1999: Further development of a hybrid-isentropic GCM. *Quart. J. Roy. Meteor. Soc.*, **125**, 2305–2331.
- Xie, P., and P. A. Arkin, 1997: Global precipitation: A 17-year monthly analysis based on gauge observations, satellite estimates, and numerical model outputs. *Bull. Amer. Meteor. Soc.*, **78**, 2539–2558.
- Zapotocny, T. H., D. R. Johnson, F. M. Reames, R. B. Pierce, and B. J. Wolf, 1991: Numerical investigations with a hybrid isentropic–sigma model. Part II: The inclusion of moist processes. *J. Atmos. Sci.*, **48**, 2025–2043.
- , —, and —, 1994: Development and initial test of the University of Wisconsin global hybrid isentropic–sigma model. *Mon. Wea. Rev.*, **122**, 2160–2178.
- , A. J. Lenzen, D. R. Johnson, F. M. Reames, P. A. Politowicz, and T. K. Schaack, 1996: Joint distributions of potential vorticity and inert trace constituent in CCM2 and UW  $\theta$ – $\sigma$  model simulations. *Geophys. Res. Lett.*, **23**, 2525–2528.
- , D. R. Johnson, T. K. Schaack, A. J. Lenzen, F. M. Reames, P. A. Politowicz, and Z. Yuan, 1997a: Simulations of tropospheric joint distributions in the UW  $\theta$ – $\sigma$  model and CCM2. *Geophys. Res. Lett.*, **24**, 865–868.
- , A. J. Lenzen, D. R. Johnson, F. M. Reames, and T. K. Schaack, 1997b: A comparison of inert trace constituent transport between the University of Wisconsin isentropic–sigma model and the NCAR Community Climate Model. *Mon. Wea. Rev.*, **125**, 120–142.
- Zhu, Z., 1997: Precipitation and water vapor transport simulated by a hybrid  $\sigma$ – $\theta$  coordinate GCM. *J. Climate*, **10**, 988–1003.
- , and E. K. Schneider, 1997: Improvement in stratosphere simulation with a hybrid  $\sigma$ – $\theta$  coordinate GCM. *Quart. J. Roy. Meteor. Soc.*, **123**, 2095–2113.
- , J. Thuburn, B. J. Hoskins, and P. H. Haynes, 1992: A vertical finite-difference scheme based on a hybrid  $\sigma$ – $\theta$ – $p$  coordinate. *Mon. Wea. Rev.*, **120**, 851–862.